JGR Biogeosciences

RESEARCH ARTICLE
10.1029/2025JG009218

Constraining Greenhouse Gas Cycling and Emissions in Africa's Largest Humic Lake

M. Barthel[1], T. W. Drake[1], A. de Clippele[1], L. W. de Groot[1], M. Engelhardt[2], N. Haghipour[2,3], Y. Hou[2], N. Kueter[2,4], D. Lewicka-Szczebak[5], A. Ludjwera Bahati[6], C. L. Tschumbu[6], K. Van Oost[7], J. N. Wabakanghanzi[8], R. A. Werner[1], J. Zambo Mandea[9], J. Six[1], and J. D. Hemingway[2]

[1]Institute of Agricultural Sciences, Department of Environmental Systems Science, ETH Zurich, Zurich, Switzerland, [2]Geological Institute, Department of Earth and Planetary Sciences, ETH Zurich, Zurich, Switzerland, [3]Laboratory for Ion Beam Physics, Department of Physics, ETH Zurich, Zurich, Switzerland, [4]Now at: Geological Institute and Institute for Petrology and Fluid Processes, Rheinisch-Westfälische Technische Hochschule Aachen, Aachen, Germany, [5]Zakład Geologii Stosowanej, Geochemii i Gospodarki Środowiskiem, Uniwersytet Wrocławski, Wroclaw, Poland, [6]Régie des Voies Fluviales, Kinshasa, Democratic Republic of Congo, [7]Earth and Life Institute, UCLouvain, Louvain-la-Neuve, Belgium, [8]Department of Soil Physics and Hydrology, Congo Atomic Energy Commission, Kinshasa, Democratic Republic of Congo, [9]Woodwell Climate Research Center, Woods Hole, MA, USA

Key Points:

- Lake Mai Ndombe is supersaturated in CO_2, CH_4, and N_2O, with outgassing fluxes of 375 ± 32 Gg C yr^{-1}, 623 ± 136 Mg C yr^{-1}, and 223 ± 20 Mg N yr^{-1} ($\mu \pm 1\sigma$)
- Up to 90% of pelagic methane is reoxidized by methanotrophic microorganisms
- Nitrous oxide is mainly formed by denitrification, with an average of 97% subsequently reduced to N_2 prior to outgassing

Supporting Information:

Supporting Information may be found in the online version of this article.

Correspondence to:

J. D. Hemingway,
jordon.hemingway@eaps.ethz.ch

Citation:

Barthel, M., Drake, T. W., de Clippele, A., de Groot, L. W., Engelhardt, M., Haghipour, N., et al. (2026). Constraining greenhouse gas cycling and emissions in Africa's largest humic lake. *Journal of Geophysical Research: Biogeosciences*, *131*, e2025JG009218. https://doi.org/10.1029/2025JG009218

Received 20 JUN 2025
Accepted 5 JAN 2026

Abstract

Humic tropical lakes and wetlands are globally important sources of atmospheric greenhouse gases (GHGs). However, mechanistic insight into GHG cycling in such systems remains limited—especially in understudied central Africa. To address this, here we measured high-, falling-, and low-water seasonal concentrations and isotopic compositions of the major dissolved GHGs CO_2, CH_4, and N_2O in Africa's largest humic lake: Mai Ndombe, Democratic Republic of Congo. We find that the water column is weakly to non-stratified and is highly supersaturated with respect to atmospheric equilibrium for all GHGs across all seasons, sampling stations, and water depths. Additionally, all GHG concentrations increase steadily with increasing water depth, reflecting atmospheric gas exchange due to physical mixing in the upper water column as well as biological processes. Extrapolating these results—combined with field measurements such as temperature and wind speed—we estimate that Lake Mai Ndombe emits 375 ± 32 Gg C yr^{-1} as CO_2, 623 ± 136 Mg C yr^{-1} as CH_4, and 223 ± 20 Mg N yr^{-1} as N_2O ($\mu \pm 1\sigma$ propagated Monte Carlo uncertainty). Furthermore, carbon-isotope signals suggest that CO_2 is largely sourced from respiration of bioavailable organic carbon, whereas CH_4 reflects sedimentary methanogenesis followed by aerobic methanotrophy in the water column. Finally, N_2O bulk and position-specific isotopic compositions reveal a nitrogen cycle dominated by sedimentary denitrification, with near-quantitative reduction to N_2 prior to upward diffusion into the water column and eventual outgassing. Combined, these observations reveal that carbon inputs, total water depth, and/or dissolved oxygen saturation are the major drivers of the flux and composition of GHGs emitted from Lake Mai Ndombe and potentially other tropical humic lakes.

Plain Language Summary

Constraining natural and anthropogenic emissions of greenhouse gases to the atmosphere is critical for understanding Earth's climate and carbon cycle. Beyond carbon dioxide, methane and nitrous oxide are powerful greenhouse gases that can be produced by microbes living in oxygen-poor environments. Organic-carbon rich ("humic") tropical lakes and wetlands are major natural sources of methane and nitrous oxide, but the underlying mechanisms and resulting importance of these emissions—particularly in understudied regions such as central Africa—are not well known. Here, we measured carbon dioxide, methane, and nitrous oxide concentrations and isotopic compositions in the largest humic lake in Africa, Lake Mai Ndombe, Democratic Republic of Congo. We show that the concentrations of all greenhouse gases in the lake water are higher than expected if in equilibrium with the atmosphere, indicating significant production within the lake system. Further, isotopic data imply that most methane and nitrous oxide that is originally produced in sediments is subsequently consumed by microbes before reaching the atmosphere. We nevertheless observe large outgassing emissions despite such high consumption rates. Combined, this implies that small perturbations to humic lake depth, dissolved oxygen content, and microbial communities could have profound impacts on the amount of greenhouse gases emitted from these systems.

1. Introduction

Relative to their surface area, inland waters—i.e., rivers, lakes, and wetlands—exert a disproportionate influence on the global carbon cycle (Lauerwald et al., 2023b; Rosentreter et al., 2021; Tian et al., 2023; Zheng et al., 2022). In particular, they transport, store, and process both inorganic and organic carbon (OC), and they serve as both short- and long-term sinks of terrestrial carbon from landscapes (Cole et al., 2007; Tranvik et al., 2009). This importance has been increasingly recognized in recent years; for example, Tian et al. (2023) estimated that nearly half of the net land carbon sink is recycled and exported through inland waters.

Such recycling leads to significant emissions of greenhouse gases (GHGs) such as carbon dioxide (CO_2), methane (CH_4), and nitrous oxide (N_2O) from inland waters. Although predictions of GHG emission fluxes continue to rise as new data are generated (Drake, Raymond, & Spencer, 2018), recent compilations have estimated that rivers and lakes emit ∼1,500 Tg C yr^{-1} as CO_2, ∼75 Tg C yr^{-1} as CH_4, and ∼0.2 to 0.8 Tg N yr^{-1} as N_2O globally (1 Tg = 10^{12} g; Lauerwald et al., 2023b; Saunois et al., 2020; Tian et al., 2020). When converted to CO_2 equivalent global warming potential (CO_2e; 100-year timescale including indirect effects; Myhre et al., 2013), these fluxes are equal to ∼20% of anthropogenic emissions in recent years (DelSontro et al., 2018), highlighting the importance of inland waters in global GHG budget estimates. Still, large discrepancies exist between top-down and bottom-up methods of quantifying global land-atmosphere carbon exchange, largely due to uncertainties in inland water emissions fluxes (Casas-Ruiz et al., 2023; Lauerwald et al., 2023a). Accurate and comprehensive inclusion of lateral carbon fluxes through inland waters is thus essential for reconciling these differences (Casas-Ruiz et al., 2023; Ciais et al., 2021).

While rivers and streams dominate inland-water CO_2 outgassing fluxes (e.g., Drake, Raymond, & Spencer, 2018), natural lakes and wetlands likely play the largest role in terms of CH_4 emissions, whereas N_2O can display either in- or outgassing behavior depending on the exact lake or river being studied (Lauerwald et al., 2023b; Zheng et al., 2022). For example, Borges et al. (2022) reported that tropical African lakes emit CH_4, but they are on average neutral with respect to N_2O fluxes since outgassing in some regions is balanced by undersaturation and ingassing in large, oligotrophic systems. Despite this complexity, some general trends have emerged: a meta-analysis of 168 lakes across several climate zones concluded that lacustrine CO_2 and N_2O emissions are generally higher in the dry relative to wet season, whereas CH_4 emissions exhibit the opposite behavior (S. Wang et al., 2024). Furthermore, lacustrine GHG emissions—particularly in low-latitude tropical systems—will likely rise with ongoing anthropogenic climate change; for example, Marotta et al. (2014) predicted a 9%–61% increase in tropical lake CO_2 and CH_4 emissions in 2100 relative to today. Despite this importance, our current understanding of GHG emissions from natural lakes remains limited—particularly in tropical, dissolved organic carbon (DOC)-rich systems (so-called "humic" lakes) that are logistically difficult to access but likely exhibit an outsize importance as GHG hotspots.

To provide new insight, we investigated GHG cycling in Lake Mai Ndombe, the largest humic lake in Africa. Mai Ndombe—meaning "black water" in the Kikongo language—is a ∼2,250 km^2 black-water lake located completely within the Cuvette Centrale, Congo River Basin, Democratic Republic of Congo. This shallow depression houses the world's largest tropical wetland complex, Tumba-Ngiri-Maindombe (Ramsar Convention Secretariat, 2013), which mainly consists of seasonally flooded tropical rainforest underlain by expansive peatlands (Figure 1a; Crezee et al., 2022; Dargie et al., 2017). These peatlands primarily drain into two humic lakes: Lake Tumba (∼700 km^2) to the north and Lake Mai Ndombe to the south. Both lakes are shallow (between ∼2–13 m water depth), warm (∼30°C), highly acidic (pH ∼3.5), and rich in DOC (∼15–30 mg C L^{-1}; Borges et al., 2022). Warm and carbon-rich conditions promote extensive in situ OC remineralization, leading to anoxic sediments and suboxic water (∼60%–80% saturation) despite an unstratified water column and extensive atmospheric gas exchange due to wind-driven physical mixing.

Rapid respiration and sub-to anoxic environments drive extensive GHG production. Although data are limited, lakes Tumba and—especially—Mai Ndombe likely exhibit the highest biogenic GHG emissions yields of any lakes in Africa (Tumba: ∼12 mol CO_2e m^{-2} yr^{-1}; Mai Ndombe: ∼28 mol CO_2e m^{-2} yr^{-1}; Borges et al., 2022). Still, despite their role as GHG hotspots, to the best of our knowledge there currently exist only a single published GHG concentration data point (collected between the falling-water stage from surface waters; Figure S1 in Supporting Information S1; Borges et al., 2022) and no in-depth biogeochemical studies for either lake. To fill this knowledge gap, in this study we first report high-, falling- and low-water seasonal water-column CO_2, CH_4, and

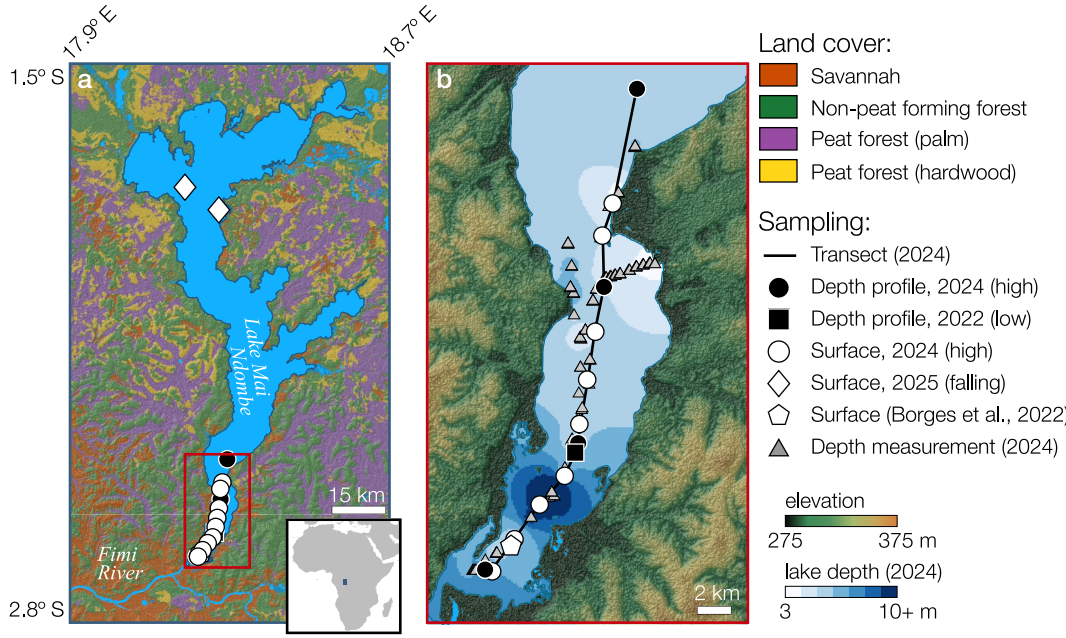

Figure 1. Lake Mai Ndombe region map. (a) Whole-lake extent, including surrounding landcover as classified by Crezee et al. (2022) as well as locations of our high-, falling-, and low-water season surface (white markers) and depth-profile (black-markers) samples and the location of a single surface sampling point from Borges et al. (2022) (white pentagon). (b) Zoomed-in view of the southern arm, including depth measurement locations (gray triangles) and predicted bathymetry as well as surrounding elevation as determined by the NASA Shuttle Radar Topography Mission (2013). Bathymetry was interpolated from measured points (high-water season 2024) using an inverse distance weighted scheme; while extrapolation of transect depths may introduce error—particularly along the East-West axis—measured values are predominantly in the 4–5 m range, suggesting little spatial water-depth variability (note: depth colorscale ends at 10 m as only a single point exceeded this value). Extent of panel (a) corresponds to blue box in whole-Africa inset; extent of panel (b) corresponds to red box in panel (a).

N_2O concentrations and isotopic compositions (i.e., $\delta^{13}C$ of CO_2 and CH_4; $\delta^{15}N^{bulk}$, $\delta^{15}N^{SP}$, and $\delta^{18}O$ of N_2O) from several sampling stations located in the northern and southern arms of Lake Mai Ndombe (Figure 1). We then model fluxes and isotopic compositions to provide mechanistic insight into GHG sources, sinks, and cycling. Finally, we predict how these processes may respond to ongoing climate change and highlight remaining open questions that would benefit from further GHG monitoring in this region.

2. Materials and Methods

2.1. Site Description and Sample Collection

Lake Mai Ndombe (Mai-Ndombe province, Democratic Republic of Congo) is located entirely within the Tumba-Ngiri-Maindombe wetland complex in the Cuvette Centrale of the Congo Basin. The lake is shallow (average water depth ~4 m) and north-south oriented with a length of ~135 km and a mean width of ~17 km (surface area ~2,250 km^2). It forms the lowest point of a swampy depression and is surrounded by periodically flooded equatorial forest as well as expansive areas of permanently flooded swamp forests dominated by *Raphia* spp., *Oubanguia africana*, and *Guibourtia demeusei* and underlain by several-meters-thick peat deposits (Figure 1a; Crezee et al., 2022; Dargie et al., 2017). The Lake Mai Ndombe watershed area is ~48,000 km^2 and is predominantly rain-fed (Georgiou, 2024); most major tributaries enter the lake from the north, whereas the only outflow drains from the southern-most point of the lake into the Fimi River, Kasaï River Basin (Figure 1a; Hughes & Hughes, 1992).

Sampling was conducted during two expeditions to the Kasaï River Basin in August 2022 (low-water season) and January 2024 (high-water season); Lake Mai Ndombe was reached from the south by boat via the Fimi River. To assess GHG emission spatial variability, additional sampling was conducted in the northern branch of Lake Mai Ndombe—reached by land from the city of Mbandaka—in June-July 2025 (falling-water season; defined as the

period in which lake level is declining). To estimate gas-transfer fluxes, wind speed at ~10 m above the water surface (U_{10}) was continuously monitored during the 2022 field campaign from our research vessel using an Atmos 41 "all-in-one" weather station (Meter Environment). Although the location of this logger did not identically match that of our GHG sampling stations, wind speeds in this region are spatially uniform; we therefore utilize the average of all U_{10} data collected within the Fimi Basin (10–17 August 2022) for all calculations (Table S1).

Before collecting samples, lake bathymetry was surveyed using a Garmin Striker 4 dual-beam transducer by measuring water depths at 147 locations throughout the sampling region; individual high-water season point measurements (minimum = 2.7 m, maximum = 13.0 m) were then linearly interpolated to generate a bathymetry map (Figure 1b). Based on remote sensing data combined with historical gauging data from the outflow (Figure S1 in Supporting Information S1; Table S2; Crétaux et al., 2011; Hughes & Hughes, 1992), we estimate that lake water level fluctuates by ~3 m throughout an annual hydrologic cycle. All water depths reported here thus refer to the depth at the time of sampling. In 2022, a single station located close to the lake outlet was sampled for GHG concentrations and isotopic compositions at the surface (~5 cm) and 4 m water depth. In 2024, depth-profile sampling was conducted at four additional stations throughout the southern arm of the lake; depending on water depth, samples were collected at the surface, 3, 6, and 10 m. Additional surface samples ($n = 9$) were collected along a transect of ~30 km to estimate spatial heterogeneity (Figure 1b). Finally, in 2025, two stations located close to the northern-most shore were sampled at the surface for GHG concentrations only (Figure 1a).

At each station (with the exception of 2025 stations and some 2024 transect surface-sample stations), in situ water temperature, pH, specific conductivity, dissolved oxygen (DO), fluorescent dissolved organic matter (fDOM), and turbidity (FNU) were measured at each sampling depth using a multi-probe (YSI EXO2 sonde, Xylem Analytics, USA). Two liters of water were then collected at each sampling depth using a custom-built, gas-tight Van Dorn sampler and subsampled for concentrations and/or isotopic compositions of: GHGs, dissolved inorganic carbon (DIC = $CO_{2(aq.)} + H_2CO_3 + HCO_3^- + CO_3^{2-}$), DOC, particulate organic carbon (POC), nutrients and major anions (i.e., ammonium, NH_4^+; nitrate, NO_3^-; sulfate, SO_4^{2-}; chloride, Cl^-), as well as stable-isotope compositions of water.

Finally, outgassed (i.e., diffusion plus ebullition) CH_4 was collected at a single station in the low-water season by deploying a floating chamber of known surface area and volume equipped with a Luer-Lock syringe sampling port on the lake surface and allowing CH_4 to accumulate for ~2 h. For outgassed CH_4 isotopic compositions, triplicate samples were collected from the floating chamber headspace and directly injected into pre-evacuated 12 mL exetainer vials (Labco, UK). Importantly, due to logistical constraints that limit the inclusion of large equipment when conducting fieldwork in remote regions of Central Africa, this study utilized a floating rather than an inverted funnel chamber, which would have been better suited for minimizing GHG back-diffusion (e.g., Walter et al., 2008). The large surface area of our floating chamber—combined with the long deployment time—renders this approach unsuitable for determining GHG outgassing fluxes or for characterizing isotopic compositions of outgassed CO_2 or N_2O, which would re-equilibrate with the dissolved phase (i.e., due to their relatively high Henry's law constants; Sander, 2025). In contrast, this approach is suitable for determining outgassed CH_4 isotopic compositions, as this is less prone to re-equilibration (i.e., due to its relatively low Henry's law constants; Sander, 2025) and requires long deployments to accurately capture ebullition fluxes. The single floating chamber sample collected here was thus exclusively used to determine outgassed CH_4 isotopic compositions—all other GHG data reported in this study were determined using dissolved samples.

To collect samples for dissolved GHG concentrations at all stations, a headspace equilibration method was employed in which a 60 mL syringe was filled with 30 mL of atmospheric air and 30 mL of water from the Van Dorn sampler, sealed, and shaken vigorously for 1 min following Roberts and Shiller (2015). After equilibration, ~24 mL of syringe headspace was injected into pre-evacuated 12 mL exetainer vials (Labco, UK); samples were collected in triplicate. Additional samples for bulk and position-specific isotopic compositions of dissolved N_2O were collected using a similar headspace equilibration method but with larger volumes (100 mL air, 100 mL water into a 200 mL syringe) and injected into pre-evacua 110 mL serum crimp vials sealed with 20 mm butyl injection stoppers. This process was repeated to over-pressurize vials to ~2 bar. At most stations, triplicate atmospheric air samples (~3 m above the lake surface) were also collected into 110 mL serum crimp vials for background concentration and isotopic correction.

For DIC, 6 mL of water was collected directly from the Van Dorn sampler into a syringe with no headspace, immediately filtered through a syringe-tip filter (hydrophilic 0.22 µm PTFE/L, 25 mm diameter, Avantor, USA), and injected into pre-poisoned (50 µL of 50% $ZnCl_2$), pre-acidified (50 µL H_3PO_4), and N_2-flushed 12 mL exetainer vials (Labco, UK). For each sample, triplicate vials were collected for concentrations and triplicate for $\delta^{13}C$ values. Additional samples for isotopic analysis of dissolved CH_4 were collected as described for DIC but with larger volumes (40 mL) and injected into pre-poisoned (1 mL of 50% $ZnCl_2$) and N_2-flushed serum crimp vials sealed with 20 mm butyl injection stoppers. For POC, ∼1 L of water was collected in high density polyethylene (HDPE) bottles (pre-rinsed 3× with sample water) and filtered through pre-combusted (450°C for 4 hr) and -weighed glass fiber type F filters (GF/F, 0.7 µm) using an acid-leached vacuum filter tower (Nalgene, USA). Filters were subsequently freeze dried, re-weighed, and stored for POC analysis. For all other analyses, ∼1 L of water was similarly collected in pre-rinsed HDPE bottles and filtered through polyethersulfone member filters (PES, 0.22 µm) using a teflon-lined positive pressure filtration tower. Filtrate was then aliquotted into (a) acid-leached opaque HDPE bottles and immediately acidified to pH 2 using 6 N HPLC-grade HCl for DOC analysis, (b) HDPE bottles for nutrient and major anion concentrations (left unacidified but immediately frozen upon return to ETH Zurich), and (c) 4 mL amber vials with no headspace for stable-isotope compositions of water.

2.2. Chemical Concentrations and Fluxes

2.2.1. Greenhouse Gases and Dissolved Inorganic Carbon

Headspace GHG and total DIC concentrations (after conversion to CO_2 in pre-acidified exetainer vials) were analyzed using a custom configured gas chromatograph (GC, Scion 456, Bruker Daltonics, Switzerland) combined with a CombiPAL autosampler (CTC Analytics AG, Switzerland). Instrumental hardware and software is optimized for the analysis of CO_2, CH_4, and N_2O in air samples. Briefly, the autosampler requires an overpressurized vial to allow a subsample to equalize at atmospheric pressure with minimal diffusion and dilution by ambient air during transport from vial to injection (2 mL total injection volume). After injection, samples are separated using Hayesep D packed columns in two parallel channels (1 mL injection each): In the first channel, CO_2 is quantified using a thermal conductivity dector (TCD) whereas CH_4 is quantified using a flame ionization detector (FID); He is used as a carrier gas. In the second channel, N_2O is quantified using an electron capture detector (ECD) with a 5% CH_4 in Ar (P5) mixture as carrier and make-up gas. The GC is calibrated during each sequence (144 samples total) using a suite of calibration gases, with typical long-term uncertainty for triplicate injections of ±6% for all GHGs (±1σ, relative uncertainty). Field-collected air samples were additionally analyzed as unknowns for background correction (average concentrations: $CO_2 = 470 \pm 23$ ppm; $CH_4 = 2101 \pm 50$ ppb; $N_2O = 344 \pm 14$ ppb; $n = 6$; $\mu \pm 1\sigma$). To convert headspace to dissolved concentrations in lake water, average water temperature measured using the multi-probe was used and atmospheric pressure at 293 m above sea level (masl; i.e., the average lake-surface elevation; Figure S1 in Supporting Information S1) was assumed.

Gas-transfer fluxes were then calculated following Cole and Caraco (1998) as

$$F = \alpha k H_s \left(p_{\text{meas.}} - p_{\text{eq.}}\right), \tag{1}$$

where α is a solubility enhancement factor due to dissociation (only relevant for CO_2; Wanninkhof & Knox, 1996), k is the gas-transfer velocity, H_s is the Henry's law solubility coefficient, $p_{\text{meas.}}$ is the measured partial pressure in the surface water, and $p_{\text{eq.}}$ is the expected partial pressure in surface water if in equilibrium with the atmosphere. For all calculations, $\alpha \approx 1$ since Lake Mai Ndombe is acidic and most DIC is present as CO_2; k can then be estimated as

$$k = k_{600}\left(\frac{\text{Sc}}{600}\right)^{n}, \tag{2}$$

where k_{600} is the reference gas-transfer velocity for a Schmidt number of 600 (i.e., CO_2 at 20°C), Sc is the Schmidt number of the gas of interest, and n is either $-2/3$ if the water surface is calm or $-1/2$ if waves are present (Jähne et al., 1987). Finally, potentially high wind speeds on large lakes require the use of wind speed-dependent gas-transfer velocities (e.g., Xiao et al., 2017), and several parameterizations exist to calculate k_{600} as a function of U_{10}. Here, the equation of Cole and Caraco (1998) was used:

$$k_{600} = 2.07 + 0.215U_{10}^{1.7}, \quad (3)$$

which is based on an empirical fit to data collected from several lakes. For each gas of interest, F was estimated using Equations 1–3 and allowing $p_{meas.}$ and $p_{eq.}$ to be the bootstrapped average of measured surface-water and background atmospheric compositions across all sampling campaigns; H_s and Sc were calculated following Sander (2025) and Wanninkhof (2014) using measured surface-water temperatures, as well as n and k_{600} using the bootstrapped daily average of measured U_{10} values from our weather station with a "wave cutoff" wind speed of 3–5 m s^{-1} (Table S1; Jähne et al., 1987). Because each parameter contains environmental and analytical uncertainty, all errors were propagated using a Monte Carlo approach (Supplementary Software). All gas-flux estimates are reported as $\mu \pm 1\sigma$ propagated Monte Carlo uncertainty.

2.2.2. Dissolved and Particulate Organic Carbon

DOC concentrations in filtered water samples were determined via high-temperature catalytic oxidation using a Shimadzu TOC-L Total Organic Carbon analyzer fitted with a TNM-1 module following the established methods described in Drake, Guillemette, et al. (2018). Resulting DOC concentrations are reported as the mean of at least three repliciate analyses in which the coefficient of variation was <2%, which we take here as relative analytical uncertainty. POC concentrations were determined from an aliquot of filtered lake sediments (≥ 0.7 μm), which were combusted using an Elemental Analyzer (varioMICRO cube, Elementar) coupled with a Isoprime precisION IRMS for subsequent isotopic analysis. Briefly, disks of known area were punched from GF/F filters, placed in silver capsules, and decarbonated by fumigation (12 N HCl vapor) at 60°C for 72 hr in a desiccator following Schwab et al. (2022). Samples were subsequently neutralized by fumigating with NaOH vapor at 60°C for 72 hr in a desiccator, wrapped in tin capsules, and pressed into disks.

2.2.3. Nutrients and Major Ions

Ammonium (NH_4^+) concentrations were determined colorimetrically using a salicylate–hypochlorite method (Bower & Holm-Hansen, 1980). Briefly, ammonium in the samples were reacted with salicylate and hypochlorite in the presence of nitraprusside to form indosalicylate. After full color development (1 hr in the dark), absorbance of the samples was measured at 640 nm with a UV-Vis spectrophotometer (Unicam). Major anion (Cl^-, SO_4^{2-}, NO_3^-) concentrations were measured by ion chromatography (Thermo Dionex Aquion with AG9-HC guard column and AS9-HC analytical column). Precision was estimated to be better than 3% for Cl^- and 5% for SO_4^{2-} ($\pm 1\sigma$, relative uncertainty) from replicate measurements of two samples ($n = 3$); in contrast, NO_3^- concentrations for all samples were below the detection limit of 2.3 μmolL^{-1}. Measurements of a reference material (BIGMOOSE-14, National Research Council Canada) agree with certified values within analytical uncertainties.

For a single sample collected in 2022, major cation (Na^+, Mg^{2+}, K^+, Ca^{2+}) concentrations were measured by inductively coupled plasma-mass spectrometry (ICP-MS, Thermo Element XR). To avoid matrix effects from high DOC concentrations, 10 mL of water was dried in a PTFE vial, subsequently fluxed with concentrated trace-metal grade nitric acid and hydrogen peroxide for three cycles, and re-dissolved in 2% nitric acid. Indium was added as an internal standard prior to analyses. Measurements of two reference materials (SLRS, National Research Council Canada and SGR-1, United States Geological Survey) matched certified and previously reported values within analytical uncertainties (Gladney & Roelandts, 1988). Precision was estimated to be better than 5.0% for Na^+, Mg^{2+}, K^+ and 5.5% for Ca^{2+} based on repeat measurements ($\pm 1\sigma$, relative uncertainty).

2.3. Isotopic Compositions

2.3.1. Dissolved Inorganic Carbon $\delta^{13}C$

DIC $\delta^{13}C$ values were determined from pre-poisoned and -acidified exetainer headspace CO_2 using a modified Finnigan Gasbench II periphery coupled to a Finnigan Delta^{plus}XP IRMS. Equilibrium isotope fractionation between dissolved and gaseous phase was corrected for using a mass balance approach with an equilibrium fractionation factor as reported in Zhang et al. (1995). Post-analysis offline calculation and offset, memory, and drift corrections were achieved following the "identical treatment principle" of Werner and Brand (2001). Following standard practice, all results are reported in "delta" (δ) notation in units of "permil" (‰) relative to

Vienna Pee Dee Belemnite (VPDB). Laboratory air working standard $\delta^{13}C$ values were determined at the Max Planck Institute for Biogeochemistry (Jena, Germany; Werner & Brand, 2001). Furthermore, 10 replicates each of two internal standards with different isotopic compositions (−25.65 and −30.88 ‰.VPDB) were analyzed in the beginning, middle, and end of each sequence (containing a maximum of 60 samples). Long-term measurement precision for both standards was ±0.26 ‰ (±1σ).

2.4. Dissolved Organic Carbon $\delta^{13}C$

DOC $\delta^{13}C$ values were determined after conversion to CO_2 using wet chemical oxidation following K. Yu et al. (2015). Briefly, 6 mL of lake water (representing ∼ 200 µgC) was transferred to a 12 mL exetainer and combined with 600 µL of 85% H_3PO_4 and 500 µL 0.15 M potassium persulfate ($K_2S_2O_8$). Vials were then sealed and sparged with 100 mL min^{-1} He for 5 min to remove any DIC. Vials were subsequently heated to 100°C for 1 hr, which prompts the generation of sulfate radicals that oxidize DOC to CO_2. Resulting headspace CO_2 was then analyzed for its ^{13}C composition exactly as described for DIC, above.

2.4.1. Methane $\delta^{13}C$

Headspace of serum crimp vials (for dissolved CH_4) or exetainers (for outgassed CH_4) was sub-sampled with a Hamilton gas-tight syringe and manually injected into a customized Hewlett Packard 6890 GC coupled to a Thermo Fisher Delta V isotope ratio mass spectrometer (GC-IRMS). Due to low CH_4 concentrations, relatively large injections of 10–25 mL were required. Injected gas was collected for 3 min on a Porapak™-filled quartz capillary trap cooled to −196°C then released at 150°C into an Agilent Poraplot-Q GC-column (50 m length, 0.32 mm wide bore, 10 µm film) cooled to −20°C using He as a carrier gas (3 mL min^{-1}; 5.0 grade; Linde Gas). After separating N_2, O_2, CO, and CH_4, the GC was heated to 150°C while increasing the flow rate to 6 mL min^{-1} for 30 min to fully elute CO_2 and higher-order hydrocarbons. After exiting the GC column, separated gases pass through a ceramic combustion unit consisting of NiO, CuO, and Pt wires heated to 1,050°C that is kept oxidized by bleeding in an auxiliary flow (0.025 mL min^{-1}) of 1% O_2 in He (cf., Merritt et al., 1995). Finally, combustion water was removed via a Nafion®-membrane capillary (40 cm long, 0.36 mm i.d.) exposed to an external counter flow of analytical-grade He gas; analyte gases were then introduced into the IRMS.

Samples were measured against in-house CH_4 standards originally calibrated against reference materials obtained from the Biogeochemical Laboratories at Indiana University, USA (Methane #1, #2, #3, #5, #7). Due to low concentration and limited sample amount, only one analysis per sample could be performed, and peak heights were typically ≤1 V (on the *m/z* 16 Faraday cup). To account and correct for linearity effects at small peak heights, in-house reference gas was diluted to match low signal yields. All results are similarly reported in units of permil relative to VPDB. The reproducibility of reference gases under these conditions was ±0.3 ‰ (±1σ), with a deviation from accepted values (i.e., linearity correction) averaging +1.7 ‰.

2.4.2. Nitrous Oxide $\delta^{15}N^{bulk}$, $\delta^{15}N^{SP}$, and $\delta^{18}O$

Bulk and position-specific isotopic compositions of N_2O were measured using an Elementar Trace Gas purge-and-trap preparation unit coupled to an Elementar IsoPrime100 IRMS as described in Verhoeven et al. (2019) and Gallarotti et al. (2021). Briefly, sample gas was purged from the headspace of serum crimp vials (for dissolved and background N_2O) using a double-holed needle, cryogenically trapped, and transferred to the IRMS. To handle high moisture content, the purge-and-trap system is additionally equipped with a Nafion®-membrane capillary dryer exposed to a counter-flow of analytical-grade He gas immediately downstream of the autosampler. The IRMS consists of 5 Faraday cups (*m/z* 30, 31, 44, 45, and 46) to simultaneously measure $\delta^{18}O$ as well as $^{15}N/^{14}N$ ratios of bulk N_2O ($\delta^{15}N^{bulk}$) and of the NO fragment created during source ionization, which is assumed to be equal to that of the central N atom ($\delta^{15}N^{\alpha}$). The isotopic composition of the terminal N atom ($\delta^{15}N^{\beta}$) is then determined by mass balance, and site-preference is calculated as $\delta^{15}N^{SP} = \delta^{15}N^{\alpha} - \delta^{15}N^{\beta}$.

In addition to the calibration steps described in Verhoeven et al. (2019) and Gallarotti et al. (2021), a sample of known isotopic composition (RM3A; Mohn et al., 2022) was analyzed as an unknown within each analytical session. Resulting root-mean square deviations (RMSD) from accepted values were 0.62 ‰, 0.59 ‰, and 0.34 ‰ for $\delta^{15}N^{bulk}$, $\delta^{15}N^{SP}$, and $\delta^{18}O$, respectively. Finally, the isotopic composition of dissolved N_2O—including propagated uncertainty—was calculated from measured values as

$$\delta_{\text{diss.}} = \frac{\delta_{\text{eq}} C_{\text{eq}} - \delta_{\text{bg}} C_{\text{bg}}}{C_{\text{eq}} - C_{\text{bg}}}, \quad (4)$$

where δ represents $\delta^{15}N^{bulk}$, $\delta^{15}N^{SP}$, or $\delta^{18}O$; "eq" is the measured equilibrated headspace gas; and "bg" is the average of all measured background atmosphere samples ($n = 8$). All $\delta^{15}N$ and $\delta^{18}O$ results are reported in units of permil relative to atmospheric air N_2 and Vienna Standard Mean Ocean Water (VSMOW), respectively.

2.4.3. Particulate Organic Carbon $\delta^{13}C$

Bulk POC isotope compositions were measured on GF/F filter aliquots at the Laboratory for Ion Beam Physics, ETH Zurich, after preparation and decarbonation as described above. Briefly, samples were converted to CO_2 gas using an Elementar Vario ISOTOPE select elemental analyzer (EA) and analyzed for their ^{13}C composition using an Isoprime precisION IRMS following McIntyre et al. (2017). Measurements were taken on separate aliquots from the same GF/F filters after decarbonating and neutralizing by fumigation as described above, and the number of punches were adapted to the carbon content of a given sample. All ^{13}C results are reported in units of permil relative to VPDB, with long-term precision of ±0.16 ‰ (±1σ) based on measured standards (OXAII, PHA, and atropine).

2.4.4. Water $\delta^{2}H$ and $\delta^{18}O$

Stable-isotope compositions of water were measured using a high-temperature conversion periphery (Finnigan TC/EA) coupled to a Finnigan Delta^{plus}XP IRMS via a Finnigan ConFlo III interface following the method described in Gehre et al. (2004). Briefly, 0.5 µL water is injected into the TC/EA via a CTC PAL autosampler equipped with a 10 µL gas-tight syringe (pre-washed 3×) where it is converted to H_2 and CO gases and chromatographically separated; $\delta^{2}H$ and $\delta^{18}O$ were thus measured using a single injection via "peak jumping," and samples were analyzed in triplicate. In-house standards are analyzed in each sequence identically to unknown samples and are calibrated to VSMOW and Standard Light Antarctic Precipitation (SLAP) values of 0 ‰ and −428 ‰ for $\delta^{2}H$ and 0 ‰ and −55.5 ‰ for $\delta^{18}O$, respectively (Coplen, 1988), using international water reference materials provided by the International Atomic Energy Agency (IAEA, Vienna, Austria). Post-analysis offline calculation and offset, memory, and drift correction were achieved following the "identical treatment principle" of Werner and Brand (2001). Long-term precision of in-house standards is ±0.6 ‰ for $\delta^{2}H$ and ±0.2 ‰ for $\delta^{18}O$ across all sequences (±1σ).

3. Results and Discussion

All relevant environmental and chemical water-column profiles are shown in Figure 2, and all measured field data, chemical concentrations, and isotopic compositions are reported in Table S3.

3.1. Gas-Flux Estimates

We first utilize our measured profiles of dissolved O_2, CO_2, CH_4, and N_2O partial pressures (i.e., pO_2, pCO_2, pCH_4, and pN_2O; Figures 2e–2h) to predict Lake Mai Ndombe ingassing (for O_2) and outgassing (for GHGs) fluxes (Table S4). Strong correlations between pO_2, pCO_2 ($R^2 = 0.80$; $p < 0.001$), and pN_2O ($R^2 = 0.82$; $p < 0.001$) across all seasons, sampling stations, and depths imply a shared physical control on the partial pressures of these gases; in contrast, pCH_4 is decoupled from all other gases, likely indicating the importance of water-column processing in addition to physical outgassing (Figure 3). Furthermore, we find no physicochemical- (i.e., temperature, pH, ion/nutrient concentrations) or dissolved gas- (i.e., O_2 or GHG concentration) based evidence for a strongly stratified water column in any season (Figure 2). That is, the water column never becomes anoxic, and pO_2, pCO_2, and pN_2O co-variance is not accompanied by corresponding changes in temperature or nutrient concentrations that would imply stratification or the development of a sharp chemocline. Nevertheless, weak stratification may have been present but not captured by our low-resolution depth profiling.

Our calculations yields a predicted O_2 ingassing flux of −31.0 ± 7.7 mmol O_2 m^{-2} d^{-1} and diffusive GHG outgassing fluxes of 38.1 ± 3.3 mmol CO_2 m^{-2} d^{-1}, 63.3 ± 13.8 µmol CH_4 m^{-2} d^{-1}, and 8.4 ± 0.7 µmol N_2O m^{-2} d^{-1} (Figure 4a). These results are lower—particularly for CH_4—than the only existing literature

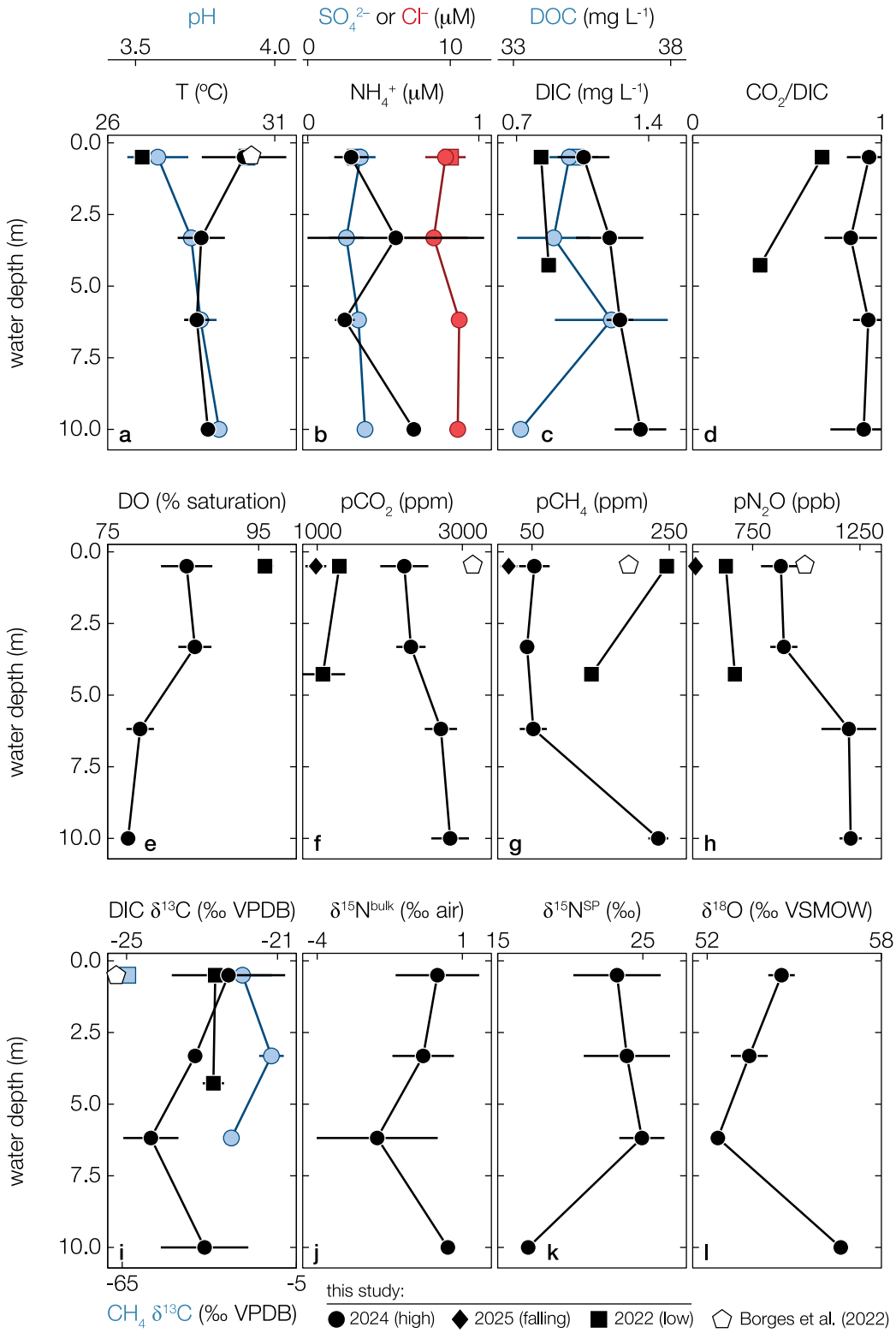

Figure 2.

estimates, which are based on a single sample collected in the falling-water season 60.2 mmol CO_2 m^{-2} d^{-1}, 180 μmol CH_4 m^{-2} d^{-1}, and 12.1 μmol N_2O m^{-2} d^{-1} (Borges et al., 2022). This difference highlights the importance of multi-season sampling, especially for CH_4 as concentrations are significantly lower in the high- and falling-water seasons relative to the low-water season (51 ± 22 ppm and 15 ± 10 ppm vs. 246 ± 25 ppm for surface samples across all sampling stations; Figure 2g). However, both our and literature predictions likely represent minimum estimates of total GHG emissions since they do not explicitly include ebullitive fluxes, which can become important for CH_4 in shallower water columns (e.g., Bastviken et al., 2010).

Assuming gas fluxes are homogeneous across the entire lake surface—which is likely reasonable given observed homogeneity in water depth, temperature, carbon inputs, and hydrology (Figure 1), as well as the strong agreement between data from our northern and southern sampling sites—we upscale these results to calculate total diffusive GHG outgassing fluxes of 375 ± 33 Gg C yr^{-1} as CO_2, 623 ± 136 Mg C yr^{-1} as CH_4, and 223 ± 20 Mg N yr^{-1} as N_2O. For context, this CO_2 outgassing flux is higher than all of the 41 globally distributed large lakes reported in Alin and Johnson (2007). When converted to CO_2e (assuming 100-year timescale and including indirect effects; Myhre et al., 2013), total predicted diffusive GHG emissions from Lake Mai Ndombe come to 408 ± 33 Gg C yr^{-1}, with CO_2 emissions contributing ∼90% of total global warming potential in this system. All flux estimates calculated here are based on two regions (i.e., northern and southern sampling) and three seasons (i.e., high-, falling-, and low-water). Still, spatial and/or temporal heterogeneity in GHG concentrations or gas-transfer velocities (i.e., wind speed), that is, not captured here could lead to biases; future work is therefore warranted to refine these flux values.

Comparing these results to current literature best estimates for all of tropical Africa, Lake Mai Ndombe accounts for ∼10% of lacustrine CO_2 emissions and a remarkable ∼50% of lacustrine N_2O emissions despite constituting only ∼1% of total lake surface area (Borges et al., 2019, 2022). Such high N_2O emissions from Lake Mai Ndombe specifically—and humic lakes more generally—may result from the fact that such systems exhibit low rates of autochthonous primary production (Borges et al., 2022), thus allowing for a greater proportion of dissolved nitrogen species to be cycled via N_2O-producing microbial processes. In contrast, Lake Mai Ndombe constitutes ≪1% of total diffusive CH_4 emissions from tropical African lakes as calculated by Borges et al. (2022). Such under-representation relative to the proportion of total lake surface area may result from either (a) an outsized importance of medium-to-large, non-humic lakes in emitting CH_4 or (b) an overestimation of total tropical African CH_4 emissions fluxes as reported in Borges et al. (2022) (e.g., es evidenced by our downward revision of Mai Ndombe CH_4 flux; Figure 4a).

3.2. Sources of Outgassed CO_2

Several concentration- and isotope-based lines of evidence indicate that DIC in Lake Mai Ndombe is predominantly sourced from OC respiration. First, pH, anion (i.e., Cl^-, SO_4^{2-}), and cation (i.e., Na^+, Mg^{2+}, K^+, Ca^{2+}) concentrations are low, averaging 3.7 ± 0.1 pH units ($n = 14$; $\mu \pm 1\sigma$), 13.4 ± 2.0 μM ($n = 12$), and 36.8 μM ($n = 1$), respectively. Although cation concentrations were only directly measured in a single sample, conductivity values are low and remarkably consistent across all seasons, locations, and water depths (50.6 ± 0.9 μS cm^{-1}; $n = 14$; $\mu \pm 1\sigma$; Table S3). Given the well-established relationship between conductivity and total dissolved solids (e.g., Rhoades, 1996), this result implies that cation concentrations are similarly low for all samples. Such low pH and ion concentrations require that most DIC is present as CO_2, as observed (Figures 2a, 2b, and 2d; $CO_2/DIC = 0.85 \pm 0.18$; $n = 13$; $\mu \pm 1\sigma$; rising to $CO_2/DIC = 0.89 \pm 0.10$ after removing one outlier).

Low ion concentrations and high CO_2/DIC ratios imply little dissolution of silicate and/or carbonate rocks in surrounding catchments, consistent with observations of deeply weathered soils, little weatherable substrate, and

Figure 2. Measured Lake Mai Ndombe depth profiles. Top row shows environmental parameters: (a) lake-water temperature and pH, (b) nutrient (NH_4^+) and major anion (SO_4^{2-}, Cl^-) concentrations, (c) DOC and DIC concentrations, and (d) fraction of total DIC present as CO_2 (CO_2/DIC). Middle row shows dissolved gas concentrations: (e) dissolved oxygen (DO), (f) CO_2, (g) CH_4, and (h) N_2O partial pressures. Bottom row shows isotopic compositions: (i) $\delta^{13}C$ of DIC and CH_4, (j) $\delta^{15}N^{bulk}$, (k) $\delta^{15}N^{SP}$, and (l) $\delta^{18}O$ of N_2O. Data are plotted as the mean and standard deviation of all samples measured at a given water depth for a given season (circles = high-water season, diamonds = falling-water season, squares = low-water season). Also shown are surface data from Borges et al. (2022) where available (white pentagons). For panels (a–c, and i), data shown with blue and red markers correspond to secondary x axes.

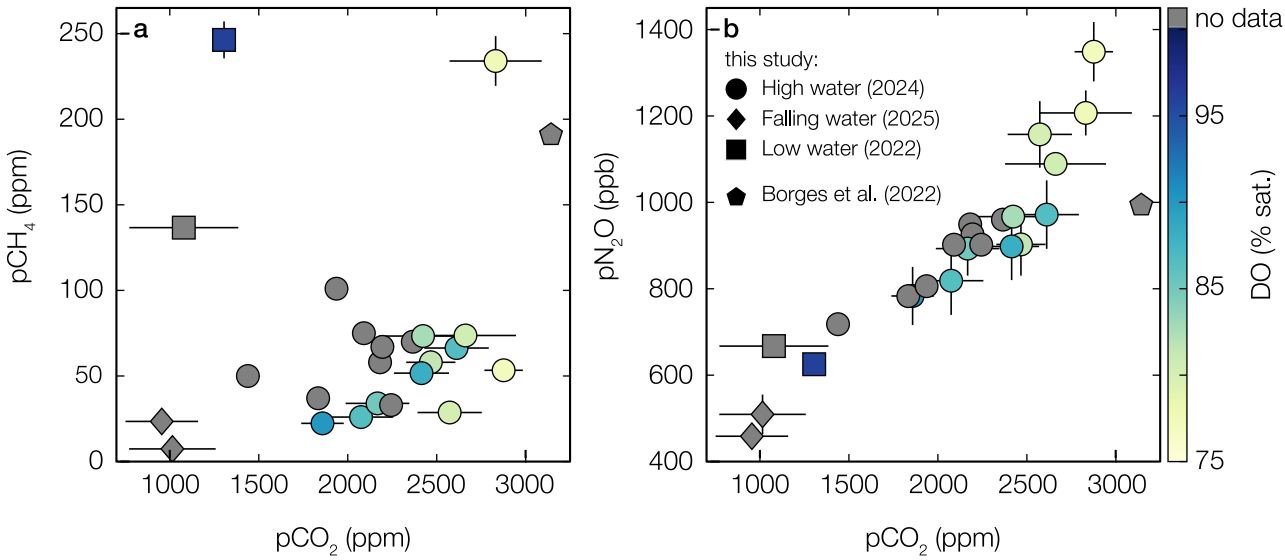

Figure 3. Gas concentration cross plots. Partial pressures of CO_2 versus (a) CH_4 and versus (b) N_2O as measured in this study (circles = high-water season, diamonds = falling-water season, squares = low-water season) and Borges et al. (2022) (pentagons). Where available, colors indicate corresponding dissolved oxygen saturation (DO, % sat.); samples with missing DO data are shown as gray markers. Strong correlations between pCO_2, pN_2O, and DO suggest water-column concentrations of all three gases are largely controlled by physical mixing with the atmosphere. In contrast, pCH_4 is decoupled, likely due to in situ consumption by aerobic methanotrophy in the water column.

thus negligible addition of DIC and alkalinity as HCO_3^-. This interpretation is supported by basin-wide observations in the Congo River, which displays some of the lowest weathering-derived ion concentrations and thus lowest area-normalized rock weathering fluxes of any major river measured to date (Gaillardet et al., 1999). Black-water rivers draining the Cuvette Centrale—which includes Lake Mai Ndombe and its surrounding watershed—display particularly low weathering fluxes, with several isotopic weathering proxies revealing that this system is dominated by secondary recycling and clay dissolution rather than input of fresh weatherable minerals (Cardinal et al., 2010; Henchiri et al., 2016). This interpretation is additionally consistent both with remote sensing data indicating that Lake Mai Ndombe is predominantly rain-water fed (Georgiou, 2024) and with our water isotope data, which reveal that lake water is isotopically identical to the global meteoric water line (GMWL; Figure S2 in Supporting Information S1). Combined, these results indicate a hydrologic setting

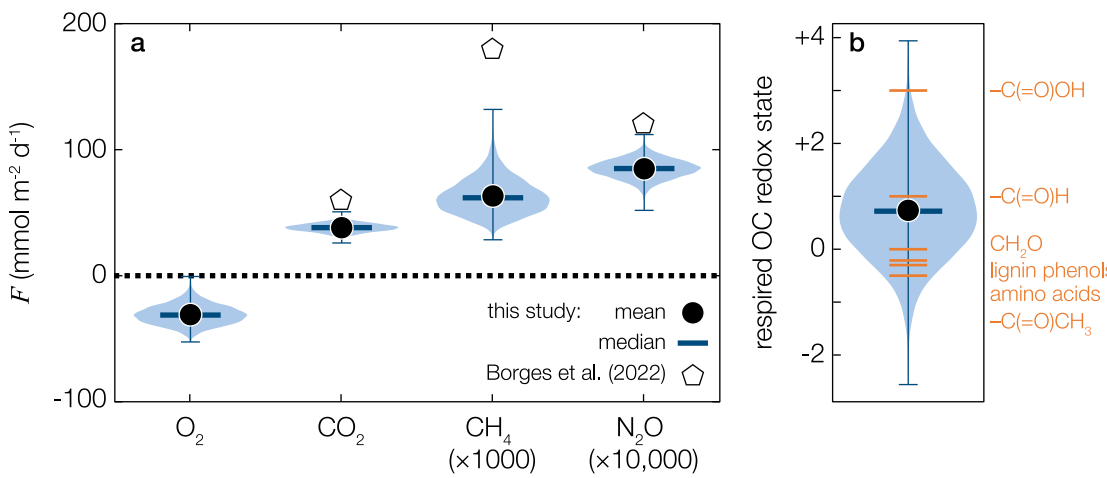

Figure 4. Predicted Lake Mai Ndombe gas fluxes and respired OC redox state. (a) Distributions (violins) of O_2, CO_2, CH_4, and N_2O gas-exchange fluxes calculated using our Monte Carlo model, where negative values indicate ingassing and vice versa. Also shown are predicted values from Borges et al. (2022) (white pentagons). Note: CH_4 and N_2O fluxes are multiplied by 1,000 and 10,000, respectively, to represent all gases on the same scale. (b) Distribution of respired OC redox state as predicted by the ratio of ingassed O_2 to outgassed CO_2 (see text for assumptions). Also shown are redox states of several common OC compounds and functional groups (orange lines and text). For both panels, black circles are distribution means, thick blue horizontal lines are medians, and thin blue whiskers are 95% confidence intervals.

dominated by repeated cycles of precipitation and (re-)evaporation, with little input from fluids such as deep groundwaters that would interact with fresh bedrock and thus little weathering-derived DIC.

Second, DIC is ^{13}C -depleted, with observed $\delta^{13}C$ values (-23.6 ± 1.3 ‰ VPDB; $n = 13$; $\mu \pm 1\sigma$; Figure 2i) approaching those of POC (-28.1 ± 1.4 ‰ VPDB, $n = 11$; $\mu \pm 1\sigma$) and DOC (-28.1 ± 0.3 ‰ VPDB, $n = 4$; $\mu \pm 1\sigma$; Table S3). Because remineralization only negligibly fractionates ^{13}C relative to starting OC, such ^{13}C -depleted signals require that DIC is predominantly sourced from respiration of organic matter, as has been observed in other tropical lowland systems (e.g., Mayorga et al., 2005). Although respiration-derived CO_2 can in theory drive silicate and/or carbonate weathering along reaction fronts in soils and deeper regolith (Brantley et al., 2023), this process is likely of minor importance here given the low observed weathering-derived ion concentrations, as discussed above. Furthermore, low $\delta^{13}C$ values imply that the ultimate source of CO_2 must be organic matter respiration, regardless of whether or not this CO_2 is transiently converted to HCO_3^- via weathering reactions (and subsequently re-protonated in low-pH, organic acid-rich waters).

Additionally, because POC concentrations in Lake Mai Ndombe (0.55 ± 0.09 mg C L^{-1}; $n = 11$; $\mu \pm 1\sigma$) represent only 1.54 ± 24 % of the total OC reservoir (i.e., POC + DOC), we conclude that DOC is likely the main substrate for OC autochthonous mineralization occurring within the lake. Water-column aerobic oxidation of methane (AeOM) may contribute additional ^{13}C -depleted DIC, although precisely quantifying the importance of this pathway to total DIC generation remains challenging. Furthermore, allochthonous respiration in surrounding soils followed by subsequent transport of CO_2-containing fluids (e.g., as overland flow or shallow groundwater) may represent a significant component of outgassed CO_2 from Lake Mai Ndombe. While $\delta^{13}C$ data included here cannot directly parse allochthonous from autochthonous respiration sources, constraining CO_2 transport pathways in the surrounding watershed represents a promising target for future studies (e.g., by including groundwater monitoring wells and/or radiocarbon analyses).

Finally, in addition to DIC production mechanisms, $\delta^{13}C$ values are further governed by the extent of CO_2 outgassing, atmospheric CO_2 equilibration, and/or in situ photosynthesis, all of which would enrich DIC in ^{13}C. While low chlorophyll a concentrations (Borges et al., 2022) indicate that in situ photosynthesis does not play a major role in Lake Mai Ndombe, we propose that atmospheric exchange and/or kinetic fractionation during outgassing leads to the observed ~4 ‰ enrichment in DIC relative to DOC and POC.

Given these DIC source predictions, the ratio of calculated O_2 ingassing and CO_2 outgassing fluxes can be used to estimate the average redox state of respired OC. Doing so requires several simplifying assumptions: (a) all outgassed CO_2 is derived from OC remineralization; (b) all remineralization is aerobic; and (c) all gas exchange occurs in Lake Mai Ndombe and the surrounding drainage network and not in unsaturated soil pores. Following these assumptions, this exercise yields an estimated OC redox state of $+0.73 \pm 0.85$ ($\mu \pm 1\sigma$; Figure 4b). While we are aware of no molecular OC data for Lake Mai Ndombe, this redox state is more oxidized than several common biosynthetic compound classes (e.g., amino acids, carbohydrates, lignin phenols) as well as ~99% of all dissolved compounds detected in the Congo River (Kurek et al., 2022).

Several possibilities could explain this difference: (i) First, respired OC in Lake Mai Ndombe may exist in a higher redox state than Congo River main-stem DOC; however, this explanation remains unlikely since respiration of POC—which is generally more hydrophobic and thus less oxidized than DOC—additionally contributes to outgassed CO_2. (ii) Second, heterotrophic organisms may preferentially respire more oxidized functional groups (e.g., carboxylic acids, aldehydes) relative to bulk OC, as has been observed in temperate and boreal lakes (Kellerman et al., 2015). This may be particularly true of humic lakes such as Lake Mai Ndombe, as OC is dominated by humic acids which contain significant amounts of oxidizied, acidic functional groups (Bade et al., 2004). (iii) Third, some outgassed CO_2 may not be balanced by ingassed O_2; this would result either if respiration occurs in soil pores using atmospheric—rather than dissolved—O_2 and/or utilizes a non-O_2 terminal electron acceptor (e.g., as expected for AeOM; Templeton et al., 2006). (iv) Finally, our gas-flux estimates may be biased toward low O_2 ingassing (i.e., high dissolved O_2 concentrations) and/or high CO_2 outgassing fluxes (i.e., high dissolved CO_2 concentrations; Figure 4a; cf., Borges et al., 2022).

As discussed above, allochthonous soil respiration and subsequent transport may contribute an unknown fraction of outgassed CO_2; we therefore consider explanation (iii) to likely be the most significant. Although not possible given the data presented here, comparing only autochthonous respiration-derived CO_2 outgassing with O_2

ingassing flux would yield more reduced OC redox-state estimates, potentially consistent with those observed in the Congo River (Kurek et al., 2022). Given these uncertainties, future landscape-scale CO_2 transport and DOC molecular-level work is therefore required to more precisely constrain the compositional source of respired OC. Nevertheless, the observation that CO_2 to O_2 flux ratios calculated here yield reasonable respired OC redox-state predictions lends credence to the validity of our overall approach.

3.3. Methane Sources, Sinks, and Cycling

Although data are limited, water-column CH_4 shows clear seasonal isotopic patterns, with ^{13}C -enriched compositions in the high-water season and ^{13}C -depleted compositions in the low-water season, with the latter nearly identical to the global wetland average value of -61.3 ± 0.7 ‰ VPDB ($\mu \pm 1\sigma$; Figure 2i; Oh et al., 2022). If we assume that bubble transfer through the water column is rapid and thus ebullitive CH_4 isotopic compositions accurately represent those of sedimentary methanogenesis (Borges et al., 2019; Conrad et al., 2011), then near identical dissolved and ebullitive $\delta^{13}C$ values in the low-water season suggest little to no AeOM at this time. In contrast, water-column AeOM during the high-water season likely drives CH_4 ^{13}C enrichment and decoupling of pCH_4 from that of other dissolved gases (Figure 3a). Indeed, substantial methanotrophy has been reported previously in black-water rivers in both the Amazon and Congo basins (Borges et al., 2019; Sawakuchi et al., 2016). These studies hypothesized that the observed importance of AeOM despite relatively low pCH_4 could be explained by some combination of (a) allochtonous inputs of high-affinity methanotrophs (Conrad et al., 2011), (b) decreased light inhibition of methanotrophy in humic, black-water systems (Sawakuchi et al., 2016), and (c) O_2 pumping via macrophyte root networks (Borges et al., 2019). While we did not observe macrophytes in Lake Mai Ndombe, we propose that seasonal AeOM variability likely arises from changes in total water depth, where deeper water and increased hydrostatic pressure in the high-water season hinder bubble release and increase the diffusive path length and thus residence time of dissolved CH_4 (Bastviken et al., 2010). Although not quantitative, this is supported by visual differences in bubble frequency observed between low- (high frequency of bubbles) and high-water season (low frequency of bubbles) sampling campaigns.

Furthermore, if we assume that CH_4 diffusing out of sediments always exhibits a concentration equal to the highest dissolved value observed in our data set (i.e., 246 ± 11 ppm) and a $\delta^{13}C$ value identical to our floating chamber sample (i.e., -64.3 ± 0.3 ‰ VPDB), then we can estimate the expressed ^{13}C isotope effect, $^{13}\varepsilon$, for AeOM following closed-system Rayleigh fractionation as

$$^{13}\varepsilon = \frac{\ln f}{1000}\left[\ln\left(\frac{\delta^{13}C_m}{1000}+1\right) - \ln\left(\frac{\delta^{13}C_0}{1000}+1\right)\right], \quad (5)$$

where $\delta^{13}C_m$ is the measured isotopic composition of a given sample, $\delta^{13}C_0$ is the initial (i.e., ebullition) isotopic composition, and f is the fraction of initial CH_4 that remains. Because $\delta^{13}C_0$ was not directly measured in this study, we approximate it as the measured value from our floating chamber. This measurement contains a mixture of diffusive and ebullitive methane; it therefore likely represents an upper-bound limit for $\delta^{13}C_0$ (i.e., the diffusive component would be exposed to AeOM). Future work—e.g., collection of porewater dissolved gases—is thus warranted to more accurately constrain $\delta^{13}C_0$ and refine our Rayleigh model. Still, given the available data and depending on the sample being considered, this exercise yields isotope effects ranging from -12 ‰ to -35 ‰ (Figure 5a), consistent with the range of values for pure and enrichment cultures as well as natural environments reported in the literature (Figure 5a and Table S5). Interestingly, the largest isotope effect calculated for any sample measured here approximates the low cell-count limit as reported in Templeton et al. (2006). In contrast, smaller isotope effects would correspond to higher cell counts and thus faster oxidation rates, where CH_4 diffusion becomes the rate-limiting step. However, sample-specific isotope effects calculated here do not show any correlation with water-column or sampling depth, potentially indicating that our assumption of a constant starting concentration and isotopic composition is invalid. Future work is therefore necessary to directly constrain fluxes and isotopic compositions of CH_4 diffusing from sediments. Regardless of the exact cell count and oxidation rate, our results indicate that water-column AeOM is an important process that significantly lowers CH_4 emissions fluxes, particularly in the high-water season.

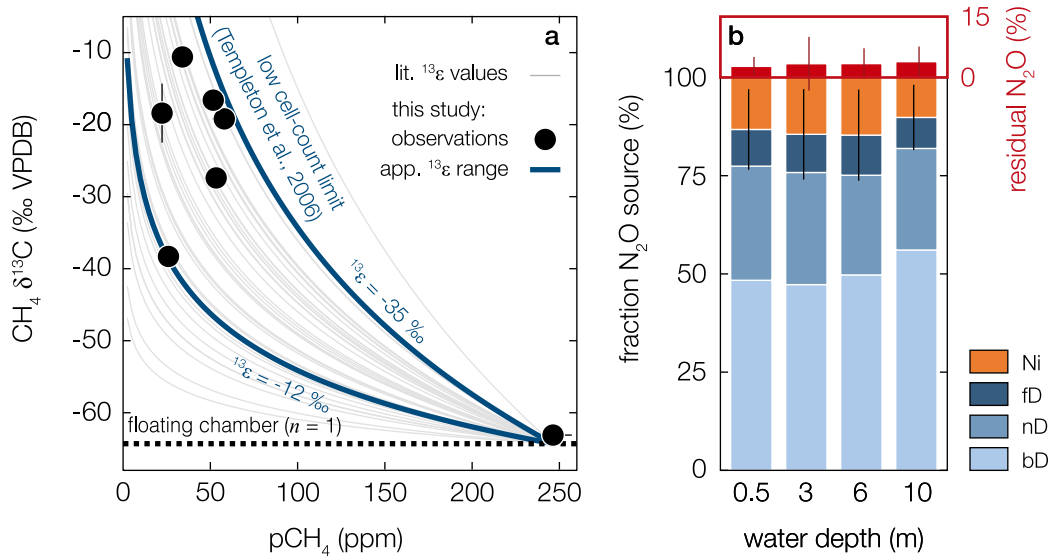

Figure 5. Isotopic evidence of GHG sources and processing. (a) Measured CH_4 $\delta^{13}C$ values as functions of pCH_4. Also shown is the $\delta^{13}C$ value of a floating chamber sample collected in August 2022 (blacked dotted line; diffusion plus ebullition). Gray lines are Rayleigh fractionation trajectories for aerobic oxidation of methane (AeOM) using several published isotope effects ($^{13}\varepsilon$) from pure and enrichment cultures as well as natural environments (Table S4; Bergamaschi et al., 1998; Coleman et al., 1981; Feisthauer et al., 2011; Happell et al., 1994; Kinnaman et al., 2007; Krause et al., 2022; Li et al., 2024; Powelson et al., 2007; Snover & Quay, 2000; Templeton et al., 2006; D. T. Wang et al., 2016) and assuming a starting composition equal to our highest measured dissolved pCH_4 sample. Thick blue lines are the calculated $^{13}\varepsilon$ values that bracket our observations. (b) Predicted N_2O source contributions as determined by an end-member mixing model based on measured $\delta^{15}N^{bulk}$, $\delta^{15}N^{SP}$, and $\delta^{18}O$ values (see text for details and assumptions; Table S5; Lewicki et al., 2022). Results are shown as the average for all samples collected at each water depth. Also shown is the model-predicted residual fraction of initial N_2O produced in sediments that is not reduced to N_2 prior to diffusion into the water column and eventual outgassing (red bars and text). Legend corresponds to: bD = bacterial denitrification, nD = nitrifier denitrification, fD = fungal denitrification, Ni = nitrification. Error bars correspond to $\pm 1\sigma$ model uncertainty on total denitrification (black) or fraction reduction (red).

3.4. Nitrous Oxide Sources, Sinks, and Cycling

Measured N_2O isotopic compositions are homogeneous across all sampling stations and water depths, averaging -0.5 ± 1.7 ‰ air for $\delta^{15}N^{bulk}$, 23.3 ± 3.1 ‰ for $\delta^{15}N^{SP}$, and 53.9 ± 1.4 ‰ VSMOW for $\delta^{18}O$ ($n = 11$; $\mu \pm 1\sigma$; Figures 2j–2l and 6). Whereas $\delta^{15}N^{SP}$ results can be explained as a mixture of several production sources (i.e., nitrification; bacterial, fungal, and nitrifier denitrification; L. Yu et al., 2020), $\delta^{15}N^{bulk}$ values are at the upper limit of those measured for bacterial denitrification, but are higher than all other potential sources. Similarly, all measured $\delta^{18}O$ values are higher than those observed for any N_2O source, suggesting significant reduction of N_2O to N_2 in a closed system (i.e., Rayleigh fractionation; Figure 6).

To better partition contributions from different N_2O production pathways—and to constrain the fraction of residual N_2O, that is, not reduced to N_2—we interpreted our $\delta^{15}N^{bulk}$, $\delta^{15}N^{SP}$, and $\delta^{18}O$ results using the Markov-Chain Monte Carlo algorithm "Fractionation And Mixing Evaluation (FRAME)" (Lewicki et al., 2022). We specifically consider N_2O production by (a) nitrification, (b) nitrifier denitrification, (c) fungal denitrification, and (d) bacterial denitrification and N_2O consumption by complete denitrification. Although recent studies have shown that photochemical production can be a large abiotic source of N_2O in both fresh and marine surface waters (Leon-Palmero et al., 2025), this process is likely of minor importance in humic lakes such as Mai Ndombe due to their high concentrations of tannic, colored DOC, which rapidly attenuates sunlight. Additionally, any associated isotope effects remain unconstrained. We therefore do not include photochemistry—nor any other potentially overlooked N_2O production pathways—in our mixing model, yet we acknowledge that results may be biased if any such processes are quantitatively important.

End-member isotopic compositions and N_2O reduction fractionation factors were largely taken from L. Yu et al. (2020) and Denk et al. (2017). For bacterial, fungal, and nitrifier denitrification end members, $\delta^{18}O$ values

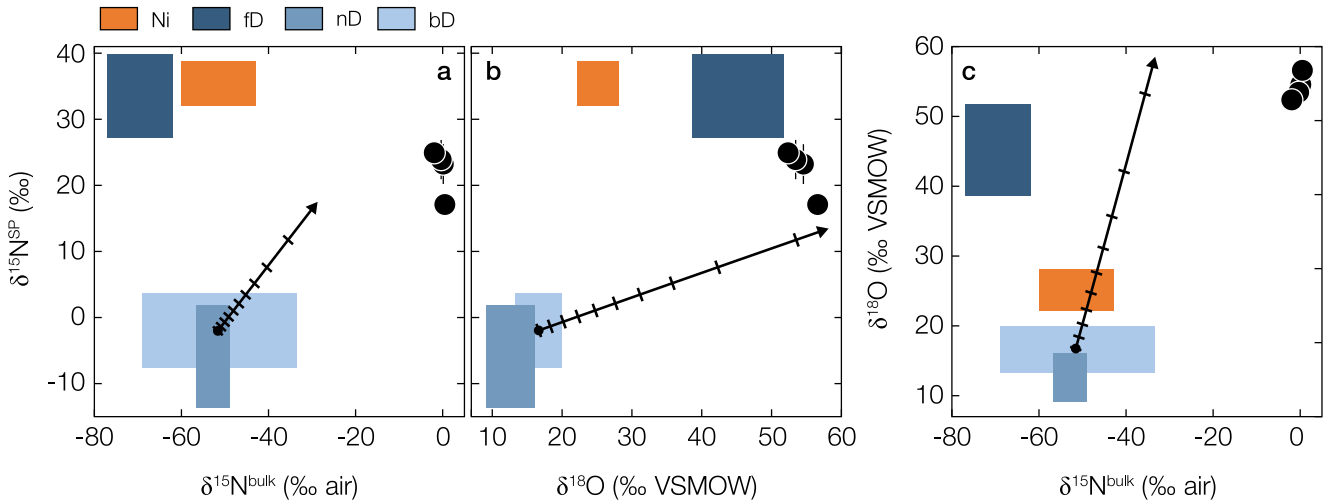

Figure 6. N_2O isotope cross-plots. Dual isotope plots showing (a) $\delta^{15}N^{bulk}$ versus $\delta^{15}N^{SP}$, (b) $\delta^{18}O$ versus $\delta^{15}N^{SP}$, and (c) $\delta^{15}N^{bulk}$ versus $\delta^{18}O$. Data are plotted as the mean and standard deviation of all samples measured at a given water depth (circles, high-water season only). Boxes indicate microbial source isotopic signatures based on pure culture studies (L. Yu et al., 2020). See main text for end-member composition determination. Also shown are dual-isotope slopes for N_2O reduction by denitrification in a closed system (i.e., Rayleigh fractionation) and arbitrarily starting from the centroid of the bacterial denitrification end-member range (black line; assuming average isotope effects of −7.1 ‰, −15.4 ‰, and −5.9 ‰ for $\delta^{15}N^{bulk}$, $\delta^{18}O$, and $\delta^{15}N^{SP}$, respectively; L. Yu et al., 2020). Tick marks correspond to 10% N_2O loss increments (i.e., residual N_2O of 90%, 80%, 70%, etc.). Legend corresponds to: bD = bacterial denitrification, nD = nitrifier denitrification, fD = fungal denitrification, Ni = nitrification.

were corrected with the known isotopic composition of lake water (Table S3). For the nitrification end member, $\delta^{18}O$ was taken as that of atmospheric O_2 with an additional enrichment due to fractionation during O_2 consumption by oxic respiration and nitrification. We specifically assume an oxygen saturation of 85 ± 8 %—the average of all values measured here (Table S3)—and a combined respiration plus nitrification isotope effect of $^{18}\varepsilon = -10$ ‰ (Levine et al., 2009). Although ^{18}O enrichment can be variable even at similar O_2 saturation values (Wassenaar, 2012), such variability is small relative to the possible end-member range. Furthermore, because $\delta^{15}N$ of NH_4^+ and NO_3^- was not measured directly in this study, we assume a value of 6.0 ‰ for substrate corrections, that is, the average value of particulate organic nitrogen from the Congo River Basin as reported in Hemingway et al. (2017). Finally, ^{15}N fractionation during mineralization of organic nitrogen ($^{15}\varepsilon = -2$ ‰; Möbius, 2013) and nitrification ($^{15}\varepsilon = -35$ ‰; Deb et al., 2024) was included when determining all end-member values. To account for natural variability, model solutions (100,000 maximum iterations, 100 burn-out Monte Carlo entries) were calculated using the average compositions for all samples collected at a given water depth, including propagated uncertainty.

Results indicate that N_2O is always predominantly sourced from bacterial and/or nitrifier denitrification, although we cannot reliably separate these end members due to their overlapping isotopic ranges (i.e., as evidenced by the strong negative correlation between their fractional estimates across Monte Carlo iterations as well as the relatively large uncertainty, averaging ±22% (±1σ) for individual denitrification pathway contributions to any individual sample; Figure 6 and Table S6). Regardless, we estimate that all denitrification sources combined contribute an average of 87^{+13}_{-16}% of N_2O at all water depths, with the remaining 13^{+16}_{-13}% sourced from nitrification (average of water-depth-specific means and 95% confidence intervals; Figure 5b and Table S6). Resulting Monte Carlo uncertainty for the nitrification contribution to any individual sample averages therefore suggests that nitrification contributions cannot be statistically differentiated from zero (Table S6). Indeed, the environmental conditions observed in Lake Mai Ndombe are known to favor denitrification, and its predominance as an N_2O source has been observed previously in other tropical rainforest soils and wetlands (Barthel et al., 2022; Fang et al., 2015; Houlton et al., 2006). Specifically, warm temperatures combined with a large influx of POC and, especially, DOC—possibly possessing an abundance of highly labile functional groups (Figure 4b)—drive rapid anoxia in sediments and thus shift microbial populations toward those that can utilize alternative terminal electron acceptors such as NO_3^-. In contrast, nitrification—particularly the oxidation of NH_4^+ to NO_2^-—is thought to be

inhibited in the low pH range typical of tropical systems (e.g., Le et al., 2019), potentially contributing to the small observed contribution of this process in Lake Mai Ndombe.

Furthermore, our FRAME results indicate that only 3^{+9}_{-3}% of all N_2O, that is, originally produced in sediments is upwardly diffused into the water column and eventually degassed without being reduced to N_2 (average of water-depth-specific means and 95% confidence intervals; Figure 5b and Table S6). Although reduction of N_2O to N_2 is commonly thought to be inhibited at low pH (e.g., Liu et al., 2014), Gallarotti et al. (2021) recently showed that *nosZ*, a marker gene encoding for this process, is present in high abundance within acidic lowland and montane soils of the Congo Basin. Marker gene-based results are consistent with our observations, which require abundant N_2O reduction despite the low in situ pH of Lake Mai Ndombe. However, it remains unclear if this process is driven by native communities present in lake sediments or by allochthonous communities derived from surrounding wetlands (i.e., analogous to the scenario hypothesized for methanotrophs; Conrad et al., 2011). Future marker-gene work in Lake Mai Ndombe sediments is therefore warranted. Still, the observation of elevated pN_2O and thus high N_2O outgassing flux (Figures 2h and 4) despite such extensive reduction to N_2 contrasts with other non-humic tropical inland waters, which are typically characterized by low pN_2O due to complete sedimentary denitrification (Borges et al., 2022). For example, Borges et al. (2019) observed a strong undersaturation of N_2O relative to atmospheric equilibrium—implying net consumption—in strongly suboxic Congolese rivers that predominantly drain swamp forest (≤25% DO saturation). We therefore predict that Lake Mai Ndombe exists in an N_2O cycling "sweet spot," with high organic inputs and anoxic sediments driving high N_2O production via denitrifiction, yet oxic to weakly suboxic water column (Figure 2e) inhibiting quantitative reduction to N_2 during upward diffusion (cf., Xie et al., 2024).

Finally, although measured values may have been impacted by potential sample-storage effects, low concentrations of both NO_3^- and NH_4^+ imply rapid and complete nitrogen cycling (Table S3). Unlike nutrient-rich aquatic systems—in which pN_2O is strongly positively related to NO_3^- and NH_4^+ concentrations—here we hypothesize that rapid overturning of process intermediates leads to low standing stocks of fixed nitrogen and an outsized importance of organic nitrogen species. This phenomenon is not limited to Lake Mai Ndombe; similar results have also been observed in other ecosystems of the Congo Basin. Specifically, Bauters et al. (2019) showed that remineralized nitrogen is largely not nitrified but rather quantitatively immobilized by microbial uptake in Congolese lowland forests and that organic nitrogen dominates over NO_3^- and NH_4^+ in streams and soil leachate. It is therefore likely that pN_2O in rivers, humic lakes, and lowland forest soils of the Congo Basin is driven mainly by a balance of dissolved oxygen content, pH, and microbial carbon source rather than standing-stock NO_3^- and NH_4^+ concentrations.

4. Conclusions

Here, we report the first in-depth investigation of GHG fluxes and cycling in Lake Mai Ndombe, DR Congo—the largest humic lake in Africa. By up-scaling surface dissolved GHG concentrations collected at 15 sampling stations across two seasons, we estimate diffusive outgassing fluxes in Lake Mai Ndombe to be 375 ± 32 Gg C yr^{-1} for CO_2, 623 ± 136 Mg C yr^{-1} for CH_4, and 223 ± 20 Mg N yr^{-1} for N_2O; combined, this corresponds to a 100-year CO_2-equivalent outgassing estimate of 408 ± 33 Gg C yr^{-1}. We further utilized stable-isotope compositions of all three GHGs to constrain their sources and sinks. We show that outgassed CO_2 is primarily sourced from oxic respiration of POC and/or DOC, and we hypothesize that remineralization of acidic, oxidized functional groups such as carboxylic acids are particularly important. In contrast, CH_4 and N_2O are primarily produced in lake sediments, with bacterial, nitrifier, and fungal denitrification contributing an estimated 87^{+13}_{-16}% of all N_2O. Both GHGs are subject to extensive secondary processing: aerobic oxidation of methane in the water column consumes up to 90% of all CH_4 diffusing out of sediments, whereas denitrification to N_2 within sediments similarly consumes 97^{+3}_{-9}% of all N_2O produced. Given such active CH_4 and N_2O cycling, small changes in water-column and sediment redox conditions—as well as total water depth—may drive large changes in GHG emissions. Overall, our first attempt for a lake-wide upscaling demonstrates that lake Mai Ndombe is a hotspot for all three major greenhouse gases. Future studies should refine these estimates by investigating spatiotemporal changes, focusing specifically on the influence of water level dynamics and inter-annual and inter-seasonal changes.

Inclusion in Global Research Statement

We thank the Régie des Voies Fluviales (RVF, DR Congo), the International Institute of Tropical Agriculture (IITA, Ibadan, Nigeria), and the Woodwell Climate Research Center (Woods Hole, Massachusetts, USA) for their partnership, facilitation, and support during all field campaigns. We thank all crew members and staff of the Kauka vessel for their dedication and guidance in navigating waterways of the Kasaï River basin. Fieldwork was conducted under research permits granted to the TropSEDs project scientific research team by the Ministère de l'Environnement et Développement Durable, DR Congo.

Conflict of Interest

The authors declare no conflicts of interest relevant to this study.

Data Availability Statement

All environmental (temperature, pH, conductivity, hydrology), concentration (DOC, DIC, ions, dissolved O_2, CH_4, N_2O, CO_2), and isotopic ($\delta^{13}C$, $\delta^{15}N^{bulk}$, $\delta^{15}N^{SP}$, $\delta^{18}O$) data as well as computational analysis scripts (written in the Python programming language) used to investigate greenhouse gas cycling in this study are available at Zenodo.org via the https://doi.org/10.5281/zenodo.15573644 with license GNU General Public License v3.0 or later (Barthel & Hemingway, 2025).

Acknowledgments

This study is part of a project that has received funding from the Swiss National Science Foundation (SNSF) under the Sinergia project "Tropical Soil Erosion Dynamics (TropSEDs)" (CRSII5_205998). J.D.H. acknowledges additional funding from the European Research Council (ERC) under the European Union's Horizon 2020 research and innovation program (Grant 946150). D.L.S. was supported by the "Polish Returns" program of the Polish National Agency of Academic Exchange (NAWA) and by the National Science Centre Poland (NCN, Grant Opus-516204). We thank Stefano M. Bernasconi for access to instrumentation and Ovide Emba for sampling the northern reaches of Lake Mai Ndombe. Open access publishing facilitated by Eidgenossische Technische Hochschule Zurich, as part of the Wiley - Eidgenossische Technische Hochschule Zurich agreement via the Consortium Of Swiss Academic Libraries.

References

Alin, S. R., & Johnson, T. C. (2007). Carbon cycling in large lakes of the world: A synthesis of production, burial, and lake-atmosphere exchange estimates. *Global Biogeochemical Cycles*, *21*(3), GB3002. https://doi.org/10.1029/2006gb002881

Bade, D. L., Carpenter, S. R., Cole, J. J., Hanson, P. C., & Hesslein, R. H. (2004). Controls of δ^{13}C-DIC in lakes: Geochemistry, lake metabolism, and morphometry. *Limnology & Oceanography*, *49*(4), 1160–1172. https://doi.org/10.4319/lo.2004.49.4.1160

Barthel, M., Bauters, M., Baumgartner, S., Drake, T. W., Bey, N. M., Bush, G., et al. (2022). Low N_2O and variable CH_4 fluxes from tropical forest soils of the Congo Basin. *Nature Communications*, *13*(1), 330. https://doi.org/10.1038/s41467-022-27978-6

Barthel, M., & Hemingway, J. D. (2025). All supplementary code used to analyze data and generate plots in Barthel et al. "Constraining greenhouse gas cycling and emissions in Africa's largest humic lake" [Dataset]. *Zenodo*. https://doi.org/10.5281/zenodo.15573644

Bastviken, D., Santoro, A. L., Marotta, H., Pinho, L. Q., Calheiros, D. F., Crill, P., & Enrich-Prast, A. (2010). Methane emissions from Pantanal, South America, during the low water season: Toward more comprehensive sampling. *Environmental Science & Technology*, *44*(14), 5450–5455. https://doi.org/10.1021/es1005048

Bauters, M., Verbeeck, H., Rütting, T., Barthel, M., Bazirake Mujinya, B., Bamba, F., et al. (2019). Contrasting nitrogen fluxes in African tropical forests of the Congo Basin. *Ecological Monographs*, *89*(1), e01342. https://doi.org/10.1002/ecm.1342

Bergamaschi, P., Lubina, C., Königstedt, R., Fischer, H., Veltkamp, A., & Zwaagstra, O. (1998). Stable isotopic signatures (δ^{13}C, δD) of methane from European landfill sites. *Journal of Geophysical Research*, *103*(D7), 8251–8265. https://doi.org/10.1029/98jd00105

Borges, A. V., Darchambeau, F., Lambert, T., Morana, C., Allen, G. H., Tambwe, E., et al. (2019). Variations in dissolved greenhouse gases (CO_2, CH_4, N_2O) in the Congo River network overwhelmingly driven by fluvial-wetland connectivity. *Biogeosciences*, *16*(19), 3801–3834. https://doi.org/10.5194/bg-16-3801-2019

Borges, A. V., Deirmendjian, L., Bouillon, S., Okello, W., Lambert, T., Roland, F. A., et al. (2022). Greenhouse gas emissions from African lakes are no longer a blind spot. *Science Advances*, *8*(25), eabi8716. https://doi.org/10.1126/sciadv.abi8716

Bower, C. E., & Holm-Hansen, T. (1980). A salicylate–hypochlorite method for determining ammonia in seawater. *Canadian Journal of Fisheries and Aquatic Sciences*, *37*(5), 794–798. https://doi.org/10.1139/f80-106

Brantley, S. L., Shaughnessy, A., Lebedeva, M. I., & Balashov, V. N. (2023). How temperature-dependent silicate weathering acts as Earth's geological thermostat. *Science*, *379*(6630), 382–389. https://doi.org/10.1126/science.add2922

Cardinal, D., Gaillardet, J., Hughes, H. J., Opfergelt, S., & André, L. (2010). Contrasting silicon isotope signatures in rivers from the Congo Basin and the specific behaviour of organic-rich waters. *Geophysical Research Letters*, *37*(12), L12403. https://doi.org/10.1029/2010gl043413

Casas-Ruiz, J. P., Bodmer, P., Bona, K. A., Butman, D., Couturier, M., Emilson, E. J., et al. (2023). Integrating terrestrial and aquatic ecosystems to constrain estimates of land-atmosphere carbon exchange. *Nature Communications*, *14*(1), 1571. https://doi.org/10.1038/s41467-023-37232-2

Ciais, P., Yao, Y., Gasser, T., Baccini, A., Wang, Y., Lauerwald, R., et al. (2021). Empirical estimates of regional carbon budgets imply reduced global soil heterotrophic respiration. *National Science Review*, *8*(2), nwaa145. https://doi.org/10.1093/nsr/nwaa145

Cole, J. J., & Caraco, N. F. (1998). Atmospheric exchange of carbon dioxide in a low-wind oligotrophic lake measured by the addition of SF_6. *Limnology & Oceanography*, *43*(4), 647–656. https://doi.org/10.4319/lo.1998.43.4.0647

Cole, J. J., Prairie, Y. T., Caraco, N. F., McDowell, W. H., Tranvik, L. J., Striegl, R. G., et al. (2007). Plumbing the global carbon cycle: Integrating inland waters into the terrestrial carbon budget. *Ecosystems*, *10*(1), 172–185. https://doi.org/10.1007/s10021-006-9013-8

Coleman, D. D., Risatti, J. B., & Schoell, M. (1981). Fractionation of carbon and hydrogen isotopes by methane-oxidizing bacteria. *Geochimica et Cosmochimica Acta*, *45*(7), 1033–1037. https://doi.org/10.1016/0016-7037(81)90129-0

Conrad, R., Noll, M., Claus, P., Klose, M., Bastos, W., & Enrich-Prast, A. (2011). Stable carbon isotope discrimination and microbiology of methane formation in tropical anoxic lake sediments. *Biogeosciences*, *8*(3), 795–814. https://doi.org/10.5194/bg-8-795-2011

Coplen, T. B. (1988). Normalization of oxygen and hydrogen isotope data. *Chemical Geology*, *72*(4), 293–297. https://doi.org/10.1016/0168-9622(88)90042-5

Crétaux, J.-F., Arsen, A., Calmant, S., Kouraev, A., Vuglinski, V., Bergé-Nguyen, M., & Maisongrande, P. (2011). SOLS: A lake database to monitor in the near real time water level and storage variations from remote sensing data. *Advances in Space Research*, *47*, 1497–1507.

Crezee, B., Dargie, G. C., Ewango, E., Corneille, Mitchard, E. T., Emba B, O., et al. (2022). Mapping peat thickness and carbon stocks of the central Congo Basin using field data. *Nature Geoscience*, *15*(8), 639–644. https://doi.org/10.1038/s41561-022-00966-7

Dargie, G. C., Lewis, S. L., Lawson, I. T., Mitchard, E. T., Page, S. E., Bocko, Y. E., & Ifo, S. A. (2017). Age, extent and carbon storage of the central Congo Basin peatland complex. *Nature*, *542*(7639), 86–90. https://doi.org/10.1038/nature21048

Deb, S., Lewicka-Szczebak, D., & Rohe, L. (2024). Microbial nitrogen transformations tracked by natural abundance isotope studies and microbiological methods: A review. *Science of the Total Environment*, *926*, 172073. https://doi.org/10.1016/j.scitotenv.2024.172073

DelSontro, T., Beaulieu, J. J., & Downing, J. A. (2018). Greenhouse gas emissions from lakes and impoundments: Upscaling in the face of global change. *Limnology and Oceanography Letters*, *3*, 64–75. https://doi.org/10.1002/lol2.10073

Denk, T. R., Mohn, J., Decock, C., Lewicka-Szczebak, D., Harris, E., Butterbach-Bahl, K., et al. (2017). The nitrogen cycle: A review of isotope effects and isotope modeling approaches. *Soil Biology and Biochemistry*, *105*, 121–137. https://doi.org/10.1016/j.soilbio.2016.11.015

Drake, T. W., Guillemette, F., Hemingway, J. D., Chanton, J. P., Podgorski, D. C., Zimov, N. S., & Spencer, R. G. (2018). The ephemeral signature of permafrost carbon in an Arctic fluvial network. *Journal of Geophysical Research: Biogeosciences*, *123*(5), 1475–1485. https://doi.org/10.1029/2017jg004311

Drake, T. W., Raymond, P. A., & Spencer, R. G. (2018). Terrestrial carbon inputs to inland waters: A current synthesis of estimates and uncertainty. *Limnology and Oceanography Letters*, *3*, 132–142. https://doi.org/10.1002/lol2.10055

Fang, Y., Koba, K., Makabe, A., Takahashi, C., Zhu, W., Hayashi, T., et al. (2015). Microbial denitrification dominates nitrate losses from forest ecosystems. *Proceedings of the National Academy of Sciences*, *112*(5), 1470–1474. https://doi.org/10.1073/pnas.1416776112

Feisthauer, S., Vogt, C., Modrzynski, J., Szlenkier, M., Krüger, M., Siegert, M., & Richnow, H.-H. (2011). Different types of methane monooxygenases produce similar carbon and hydrogen isotope fractionation patterns during methane oxidation. *Geochimica et Cosmochimica Acta*, *75*(5), 1173–1184. https://doi.org/10.1016/j.gca.2010.12.006

Gaillardet, J., Dupré, B., Louvat, P., & Allegre, C. (1999). Global silicate weathering and CO_2 consumption rates deduced from the chemistry of large rivers. *Chemical Geology*, *159*(1–4), 3–30. https://doi.org/10.1016/s0009-2541(99)00031-5

Gallarotti, N., Barthel, M., Verhoeven, E., Pereira, E. I. P., Bauters, M., Baumgartner, S., et al. (2021). In-depth analysis of N_2O fluxes in tropical forest soils of the Congo Basin combining isotope and functional gene analysis. *The ISME Journal*, *15*(11), 3357–3374. https://doi.org/10.1038/s41396-021-01004-x

Gehre, M., Geilmann, H., Richter, J., Werner, R., & Brand, W. (2004). Continuous flow $^2H/^1H$ and $^{18}O/^{16}O$ analysis of water samples with dual inlet precision. *Rapid Communications in Mass Spectrometry*, *18*(22), 2650–2660. https://doi.org/10.1002/rcm.1672

Georgiou, S. (2024). *Inundation and greenhouse gas dynamics of the central Congo Basin wetlands* (Unpublished doctoral dissertation). The University of Edinburgh.

Gladney, E. S., & Roelandts, I. (1988). 1987 compilation of elemental concentration data for USGS BHVO-1, MAG-1, QLO-1, RGM-1, SCo-1, SDC-1, SGR-1 and STM-1. *Geostandards Newsletter*, *12*(2), 253–362. https://doi.org/10.1111/j.1751-908x.1988.tb00053.x

Happell, J. D., Chanton, J. P., & Showers, W. S. (1994). The influence of methane oxidation on the stable isotopic composition of methane emitted from Florida swamp forests. *Geochimica et Cosmochimica Acta*, *58*(20), 4377–4388. https://doi.org/10.1016/0016-7037(94)90341-7

Hemingway, J. D., Schefuß, E., Spencer, R. G., Dinga, B. J., Eglinton, T. I., McIntyre, C., & Galy, V. V. (2017). Hydrologic controls on seasonal and inter-annual variability of Congo River particulate organic matter source and reservoir age. *Chemical Geology*, *466*, 454–465. https://doi.org/10.1016/j.chemgeo.2017.06.034

Henchiri, S., Gaillardet, J., Dellinger, M., Bouchez, J., & Spencer, R. G. (2016). Riverine dissolved lithium isotopic signatures in low-relief central Africa and their link to weathering regimes. *Geophysical Research Letters*, *43*(9), 4391–4399. https://doi.org/10.1002/2016gl067711

Houlton, B. Z., Sigman, D. M., & Hedin, L. O. (2006). Isotopic evidence for large gaseous nitrogen losses from tropical rainforests. *Proceedings of the National Academy of Sciences*, *103*(23), 8745–8750. https://doi.org/10.1073/pnas.0510185103

Hughes, R. H., & Hughes, J. (1992). *A directory of African wetlands*. IUCN – The World Conservation Union.

Jähne, B., Münnich, K. O., Bösinger, R., Dutzi, A., Huber, W., & Libner, P. (1987). On the parameters influencing air-water gas exchange. *Journal of Geophysical Research*, *92*, 1937–1949.

Kellerman, A. M., Kothawala, D. N., Dittmar, T., & Tranvik, L. J. (2015). Persistence of dissolved organic matter in lakes related to its molecular characteristics. *Nature Geoscience*, *8*(6), 454–457. https://doi.org/10.1038/ngeo2440

Kinnaman, F. S., Valentine, D. L., & Tyler, S. C. (2007). Carbon and hydrogen isotope fractionation associated with the aerobic microbial oxidation of methane, ethane, propane and butane. *Geochimica et Cosmochimica Acta*, *71*(2), 271–283. https://doi.org/10.1016/j.gca.2006.09.007

Krause, S. J., Liu, J., Young, E. D., & Treude, T. (2022). $\Delta^{13}CH_3D$ and $\Delta^{12}CH_2D_2$ signatures of methane aerobically oxidized by *Methylosinus trichosporium* with implications for deciphering the provenance of methane gases. *Earth and Planetary Science Letters*, *593*, 117681.

Kurek, M. R., Stubbins, A., Drake, T. W., Dittmar, T., MS Moura, J., Holmes, R. M., et al. (2022). Organic molecular signatures of the Congo River and comparison to the Amazon. *Global Biogeochemical Cycles*, *36*(6), e2022GB007301. https://doi.org/10.1029/2022gb007301

Lauerwald, R., Allen, G. H., Deemer, B. R., Liu, S., Maavara, T., Raymond, P., et al. (2023a). Inland water greenhouse gas budgets for RECCAP2: 1. state-of-the-art of global scale assessments. *Global Biogeochemical Cycles*, *37*(5), e2022GB007657. https://doi.org/10.1029/2022gb007657

Lauerwald, R., Allen, G. H., Deemer, B. R., Liu, S., Maavara, T., Raymond, P., et al. (2023b). Inland water greenhouse gas budgets for RECCAP2: 2. regionalization and homogenization of estimates. *Global Biogeochemical Cycles*, *37*(5), e2022GB007658. https://doi.org/10.1029/2022gb007658

Le, T. T. H., Fettig, J., & Meon, G. (2019). Kinetics and simulation of nitrification at various pH values of a polluted river in the tropics. *Ecohydrology and Hydrobiology*, *19*(1), 54–65. https://doi.org/10.1016/j.ecohyd.2018.06.006

Leon-Palmero, E., Morales-Baquero, R., Thamdrup, B., Löscher, C., & Reche, I. (2025). Sunlight drives the abiotic formation of nitrous oxide in fresh and marine waters. *Science*, *387*(6739), 1198–1203. https://doi.org/10.1126/science.adq0302

Levine, N. M., Bender, M. L., & Doney, S. C. (2009). The $\delta^{18}O$ of dissolved O_2 as a tracer of mixing and respiration in the mesopelagic ocean. *Global Biogeochemical Cycles*, *23*(1). https://doi.org/10.1029/2007gb003162

Lewicki, M. P., Lewicka-Szczebak, D., & Skrzypek, G. (2022). FRAME–Monte Carlo model for evaluation of the stable isotope mixing and fractionation. *PLoS One*, *17*(11), e0277204. https://doi.org/10.1371/journal.pone.0277204

Li, J., Chiu, B. K., Piasecki, A. M., Feng, X., Landis, J. D., Marcum, S., et al. (2024). The evolution of multiply substituted isotopologues of methane during microbial aerobic oxidation. *Geochimica et Cosmochimica Acta*, *381*, 223–238. https://doi.org/10.1016/j.gca.2024.06.032

Liu, B., Frostegård, Å., & Bakken, L. R. (2014). Impaired reduction of N_2O to N_2 in acid soils is due to a posttranscriptional interference with the expression of *nosZ*. *mBio*, *5*(3), 10–1128. https://doi.org/10.1128/mBio.01383-14

Marotta, H., Pinho, L., Gudasz, C., Bastviken, D., Tranvik, L. J., & Enrich-Prast, A. (2014). Greenhouse gas production in low-latitude lake sediments responds strongly to warming. *Nature Climate Change*, *4*(6), 467–470. https://doi.org/10.1038/nclimate2222

Mayorga, E., Aufdenkampe, A. K., Masiello, C. A., Krusche, A. V., Hedges, J. I., Quay, P. D., et al. (2005). Young organic matter as a source of carbon dioxide outgassing from Amazonian rivers. *Nature*, *436*(7050), 538–541. https://doi.org/10.1038/nature03880

McIntyre, C. P., Wacker, L., Haghipour, N., Blattmann, T. M., Fahrni, S., Usman, M., et al. (2017). Online ^{13}C and ^{14}C gas measurements by EA-IRMS-AMS at ETH Zürich. *Radiocarbon*, *59*(3), 893–903. https://doi.org/10.1017/rdc.2016.68

Merritt, D. A., Freeman, K. H., Ricci, M. P., Studley, S. A., & Hayes, J. (1995). Performance and optimization of a combustion interface for isotope ratio monitoring gas chromatography/mass spectrometry. *Analytical Chemistry*, *67*(14), 2461–2473. https://doi.org/10.1021/ac00110a022

Möbius, J. (2013). Isotope fractionation during nitrogen remineralization (ammonification): Implications for nitrogen isotope biogeochemistry. *Geochimica et Cosmochimica Acta*, *105*, 422–432.

Mohn, J., Biasi, C., Bodé, S., Boeckx, P., Brewer, P. J., Eggleston, S., et al. (2022). Isotopically characterised N_2O reference materials for use as community standards. *Rapid Communications in Mass Spectrometry*, *36*(13), e9296. https://doi.org/10.1002/rcm.9296

Myhre, G., Shindell, D., Bréon, F., Collins, W., Fuglestvedt, J., Huang, J., et al. (2013). Anthropogenic and natural radiative forcing. In T. F. Stocker, D. Qin, G.-K. Plattner, M. Tignor, S. K. Allen, J. Boschung, et al. (Eds.), *Climate change 2013: The physical science basis. Contribution of working group I to the fifth assessment report of the intergovernmental panel on climate change*, (pp. 659–740). Cambridge University Press.

NASA Shuttle Radar Topography Mission. (2013). https://doi.org/10.5069/G9445JDF

Oh, Y., Zhuang, Q., Welp, L. R., Liu, L., Lan, X., Basu, S., et al. (2022). Improved global wetland carbon isotopic signatures support post-2006 microbial methane emission increase. *Communications Earth & Environment*, *3*(1), 159. https://doi.org/10.1038/s43247-022-00488-5

Powelson, D., Chanton, J., & Abichou, T. (2007). Methane oxidation in biofilters measured by mass-balance and stable isotope methods. *Environmental Science & Technology*, *41*(2), 620–625. https://doi.org/10.1021/es061656g

Ramsar Convention Secretariat. (2013). *The Ramsar convention manual: A guide to the convention on wetlands (Ramsar, Iran, 1971)* (6th ed.). IUCN – The World Conservation Union.

Rhoades, J. (1996). Salinity: Electrical conductivity and total dissolved solids. *Methods of Soil Analysis: Part 3 Chemical Methods*, *5*, 417–435.

Roberts, H. M., & Shiller, A. M. (2015). Determination of dissolved methane in natural waters using headspace analysis with cavity ring-down spectroscopy. *Analytica Chimica Acta*, *856*, 68–73. https://doi.org/10.1016/j.aca.2014.10.058

Rosentreter, J. A., Borges, A. V., Deemer, B. R., Holgerson, M. A., Liu, S., Song, C., et al. (2021). Half of global methane emissions come from highly variable aquatic ecosystem sources. *Nature Geoscience*, *14*(4), 225–230. https://doi.org/10.1038/s41561-021-00715-2

Sander, R. (2025). Henry's law constants. In P. J. Linstrom & W. G. Mallard (Eds.), *NIST chemistry WebBook, NIST standard reference database number 69*. National Institute of Standards and Technology. https://doi.org/10.18434/T4D303

Saunois, M., Stavert, A., Poulter, B., Bousquet, P., Canadell, J., Jackson, R., et al. (2020). The global methane budget 2000–2017. *Earth System Science Data*, *12*(3), 1561–1623. https://doi.org/10.5194/essd-12-1561-2020

Sawakuchi, H. O., Bastviken, D., Sawakuchi, A. O., Ward, N. D., Borges, C. D., Tsai, S. M., et al. (2016). Oxidative mitigation of aquatic methane emissions in large Amazonian rivers. *Global Change Biology*, *22*(3), 1075–1085. https://doi.org/10.1111/gcb.13169

Schwab, M. S., Gies, H., Freymond, C. V., Lupker, M., Haghipour, N., & Eglinton, T. I. (2022). Environmental and hydrologic controls on sediment and organic carbon export from a subalpine catchment: Insights from a time series. *Biogeosciences*, *19*(23), 5591–5616. https://doi.org/10.5194/bg-19-5591-2022

Snover, A. K., & Quay, P. D. (2000). Hydrogen and carbon kinetic isotope effects during soil uptake of atmospheric methane. *Global Biogeochemical Cycles*, *14*(1), 25–39. https://doi.org/10.1029/1999gb900089

Templeton, A. S., Chu, K.-H., Alvarez-Cohen, L., & Conrad, M. E. (2006). Variable carbon isotope fractionation expressed by aerobic CH_4-oxidizing bacteria. *Geochimica et Cosmochimica Acta*, *70*(7), 1739–1752. https://doi.org/10.1016/j.gca.2005.12.002

Tian, H., Xu, R., Canadell, J. G., Thompson, R. L., Winiwarter, W., Suntharalingam, P., et al. (2020). A comprehensive quantification of global nitrous oxide sources and sinks. *Nature*, *586*(7828), 248–256. https://doi.org/10.1038/s41586-020-2780-0

Tian, H., Yao, Y., Li, Y., Shi, H., Pan, S., Najjar, R. G., et al. (2023). Increased terrestrial carbon export and CO_2 evasion from global inland waters since the preindustrial era. *Global Biogeochemical Cycles*, *37*(10), e2023GB007776. https://doi.org/10.1029/2023gb007776

Tranvik, L. J., Downing, J. A., Cotner, J. B., Loiselle, S. A., Striegl, R. G., Ballatore, T. J., et al. (2009). Lakes and reservoirs as regulators of carbon cycling and climate. *Limnology & Oceanography*, *54*(6part2), 2298–2314. https://doi.org/10.4319/lo.2009.54.6_part_2.2298

Verhoeven, E., Barthel, M., Yu, L., Celi, L., Said-Pullicino, D., Sleutel, S., et al. (2019). Early season N_2O emissions under variable water management in rice systems: Source-partitioning emissions using isotope ratios along a depth profile. *Biogeosciences*, *16*(2), 383–408. https://doi.org/10.5194/bg-16-383-2019

Walter, K., Chanton, J., Chapin Iii, F., Schuur, E., & Zimov, S. (2008). Methane production and bubble emissions from arctic lakes: Isotopic implications for source pathways and ages. *Journal of Geophysical Research*, *113*(G3), JG000569. https://doi.org/10.1029/2007jg000569

Wang, D. T., Welander, P. V., & Ono, S. (2016). Fractionation of the methane isotopologues $^{13}CH_4$, $^{12}CH_3D$, and $^{13}CH_3D$ during aerobic oxidation of methane by *Methylococcus capsulatus* (bath). *Geochimica et Cosmochimica Acta*, *192*, 186–202. https://doi.org/10.1016/j.gca.2016.07.031

Wang, S., Wu, S., Dong, Y., Li, X., Wang, Y., Li, Y., et al. (2024). River-lake ecosystems exhibit a strong seasonal cycle of greenhouse gas emissions. *Communications Earth & Environment*, *5*(1), 784. https://doi.org/10.1038/s43247-024-01912-8

Wanninkhof, R. (2014). Relationship between wind speed and gas exchange over the ocean revisited. *Limnology and Oceanography: Methods*, *12*(6), 351–362. https://doi.org/10.4319/lom.2014.12.351

Wanninkhof, R., & Knox, M. (1996). Chemical enhancement of CO_2 exchange in natural waters. *Limnology & Oceanography*, *41*(4), 689–697. https://doi.org/10.4319/lo.1996.41.4.0689

Wassenaar, L. I. (2012). Dissolved oxygen status of Lake Winnipeg: Spatio-temporal and isotopic ($\delta^{18}O-O_2$) patterns. *Journal of Great Lakes Research*, *38*, 123–134. https://doi.org/10.1016/j.jglr.2010.12.011

Werner, R. A., & Brand, W. A. (2001). Referencing strategies and techniques in stable isotope ratio analysis. *Rapid Communications in Mass Spectrometry*, *15*(7), 501–519. https://doi.org/10.1002/rcm.258

Xiao, Q., Zhang, M., Hu, Z., Gao, Y., Hu, C., Liu, C., et al. (2017). Spatial variations of methane emission in a large shallow eutrophic lake in subtropical climate. *Journal of Geophysical Research: Biogeosciences*, *122*(7), 1597–1614. https://doi.org/10.1002/2017jg003805

Xie, S., Xia, T., Li, H., Chen, Y., & Zhang, W. (2024). Variability in N_2O emission controls among different ponds within a hilly watershed. *Water Research*, *267*, 122467. https://doi.org/10.1016/j.watres.2024.122467

Yu, K., Gan, Y., Zhou, A., Han, L., & Liu, Y. (2015). A persulfate oxidation method for stable isotope analysis of dissolved organic carbon and the influence of inorganic ions on the results. *International Journal of Mass Spectrometry*, *392*, 63–68. https://doi.org/10.1016/j.ijms.2015.09.006

Yu, L., Harris, E., Lewicka-Szczebak, D., Barthel, M., Blomberg, M. R., Harris, S. J., et al. (2020). What can we learn from N_2O isotope data? Analytics, processes and modelling. *Rapid Communications in Mass Spectrometry*, *34*(20), e8858. https://doi.org/10.1002/rcm.8858

Zhang, J., Quay, P., & Wilbur, D. (1995). Carbon isotope fractionation during gas-water exchange and dissolution of CO_2. *Geochimica et Cosmochimica Acta*, *59*(1), 107–114. https://doi.org/10.1016/0016-7037(95)91550-d

Zheng, Y., Wu, S., Xiao, S., Yu, K., Fang, X., Xia, L., et al. (2022). Global methane and nitrous oxide emissions from inland waters and estuaries. *Global Change Biology*, *28*(15), 4713–4725. https://doi.org/10.1111/gcb.16233

References From the Supporting Information

Craig, H. (1961). Isotopic variations in meteoric waters. *Science*, *133*(3465), 1702–1703. https://doi.org/10.1126/science.133.3465.1702

Ndembo, L., Travi, Y., Moyengo, L., & Wabakaghanzi, J. (2007). Isotopes in precipitations of Kinshasa area: Moisture sources and groundwater tracing. *Advances in Isotope Hydrology and its Role in Sustainable Water Resources Management (IHS—2007)*, *1*, 279–288.